



저작자표시-비영리-변경금지 2.0 대한민국

이용자는 아래의 조건을 따르는 경우에 한하여 자유롭게

- 이 저작물을 복제, 배포, 전송, 전시, 공연 및 방송할 수 있습니다.

다음과 같은 조건을 따라야 합니다:



저작자표시. 귀하는 원저작자를 표시하여야 합니다.



비영리. 귀하는 이 저작물을 영리 목적으로 이용할 수 없습니다.



변경금지. 귀하는 이 저작물을 개작, 변형 또는 가공할 수 없습니다.

- 귀하는, 이 저작물의 재이용이나 배포의 경우, 이 저작물에 적용된 이용허락조건을 명확하게 나타내어야 합니다.
- 저작권자로부터 별도의 허가를 받으면 이러한 조건들은 적용되지 않습니다.

저작권법에 따른 이용자의 권리는 위의 내용에 의하여 영향을 받지 않습니다.

이것은 [이용허락규약\(Legal Code\)](#)을 이해하기 쉽게 요약한 것입니다.

[Disclaimer](#)

의학박사 학위논문

Predictive model for
fluorodeoxyglucose avidity in
gastric cancer using
patient-derived xenograft
model as an imaging
biomarker

환자유래 이종이식 모델을 이용한
위암에서 이미징 바이오마커로써
FDG 친화력 예측 모델

2020년 8월

서울대학교 대학원
의학과 협동과정 종양생물학 전공
배 성 우

A Thesis of the Degree of Doctor of
Philosophy

**환자유래 이종이식 모델을 이용한
위암에서 이미징 바이오마커로써
FDG 친화력 예측 모델**

Predictive model for fluorodeoxyglucose
avidity in gastric cancer using
patient-derived xenograft model as an
imaging biomarker

August 2020

Interdisciplinary Program in Cancer
Biology

Seoul National University

College of Medicine

Seong-Woo Bae

**Predictive model for fluorodeoxyglucose
avidity in gastric cancer using
patient-derived xenograft model as an
imaging biomarker**

**by
Seong-Woo Bae**

**A thesis submitted to the Interdisciplinary Program
in partial fulfillment of the requirements
for the Degree of Doctor of Philosophy in Cancer
Biology at Seoul National University College of
Medicine**

July, 2020

Approved by Thesis Committee:

Professor _____Chairman
Professor _____Vice chairman
Professor _____
Professor _____
Professor _____

환자유래 이중이식 모델을 이용한 위암에서 이미징 바이오마커로써 FDG 친화력 예측 모델

지도교수 양한광

이 논문을 의학박사 학위논문으로 제출함
2020 년 5 월

서울대학교 대학원
의학과 협동과정 종양생물학 전공
배 성 우

배성우의 의학박사 학위논문을 인준함
2020 년 7 월

위 원 장	_____	(인)
부 위 원 장	_____	(인)
위 원	_____	(인)
위 원	_____	(인)
위 원	_____	(인)

ABSTRACT

Seong-Woo Bae

Interdisciplinary Program in Cancer Biology

The Graduate School

Seoul National University

Background: Although fluorodeoxyglucose positron emission tomography (FDG-PET) is widely used in staging, response monitoring and evaluating recurrence for various cancers, its role in gastric cancer (GC) is still limited due to variable FDG avidity of malignant lesions. Patient derived-xenograft (PDX) models, as patient surrogates, are considered promising *in-vivo* models in preclinical research. The purpose of this study is to develop a gene signature to predict FDG avidity in GC based on established PET imaging PDX murine models to plan individualized PET and investigate the molecular characteristic landscape.

Methods: Female BALB/c nu/nu mice were implanted orthotopically and subcutaneously with GC PDX tissues. [¹⁸F]FDG-PET scanning protocol evaluation included different tumor sizes, FDG doses, scanning intervals and organ specific uptake. FDG avidity of similar PDX cases

were compared between orthotopic and heterotopic tumor implantation models. Microscopic and immunohistochemical investigations were performed to confirm tumor growths and correlate protein expressions of glucose transporter 1 (GLUT1) and hexokinase 2 (HK2) with FDG uptake.

Using RNA sequencing data of thirty PDX cases paired with FDG-PET results, we identified a five-gene signature (*PLS1*, *PYY*, *HBQ1*, *SLC6A5*, *NAT16*) associated with the maximum standardized uptake value (SUVmax). We established a model (PETscore) for predicting high FDG-avid GC using the signature, which was validated in human by RNA-seq and qRT-PCR. Furthermore, we also characterized the model using public data of GC profiled in The Cancer Genome Atlas (TCGA) and Asian Cancer Research Group (ACRG).

Results: PET scanning protocol was determined to include 150 μ Ci FDG injection dose and scanning after one hour. Comparison of heterotopic and orthotopic implanted mouse models revealed longer growths interval for orthotopic models with higher uptake in similar PDX tissues. H-scores of GLUT1 and HK2 expressions in tumor cells were correlated with measured SUVmax values. Validation of PETscore provided significant predictive values compared with actual SUVmax in human. Investigation with TCGA and ACRG data showed that the PETscore was significantly associated with glycolysis, microsatellite instability (MSI) status and epithelial mesenchymal transition (EMT)-related prognosis.

Conclusion: This preclinical GC PDX based [^{18}F]FDG-PET protocol reveals tumor specific FDG uptake and shows correlation to glucose metabolic proteins. PDX transplanted mouse model can be useful to access PET activity in gastric cancer. Our findings in study for FDG avidity prediction model suggest the molecular characteristics of GC underlying the diverse metabolic profiles. Furthermore, our PETscore could be proposed for an individualized FDG-PET for staging and disease monitoring by predicting FDG avidity.

Keywords: Gastric cancer, Positron emission tomography, Patient-derived xenograft, Gene signature, Standardized uptake value, Glycolysis, Microsatellite instability, Epithelial mesenchymal transition

Student number: 2017-34897

CONTENTS

ABSTRACT.....	i
CONTENTS.....	iv
LIST OF TABLES AND FIGURES.....	v
INTRODUCTION.....	1
PART I. Establishment of protocol for preclinical PET imaging of human gastric cancer PDX models	
MATERIAL AND METHODS.....	5
RESULTS.....	13
PART II. Development of prediction model with a gene signature for FDG avidity in gastric cancer	
MATERIAL AND METHODS.....	26
RESULTS.....	39
DISCUSSION.....	70
REFERENCES.....	81
ABSTRACT IN KOREAN.....	91

LIST OF TABLES AND FIGURES

PART I. Establishment of protocol for preclinical PET imaging of human gastric cancer PDX models

Table 1. Clinico-pathological characteristics of the donor patients

Table 2. Summary of successful rate between heterotopic and orthotopic models

Figure 1. Orthotopic xenograft model of gastric cancer PDX

Figure 2. Selection of optimal tumor size for [^{18}F]FDG PET imaging protocol

Figure 3. Selection of optimal dose for [^{18}F]FDG PET imaging protocol

Figure 4. Injection dose selection for PET imaging protocol from the theoretical decay curve of F-18

Figure 5. Inflammatory PET signal aspect for orthotopic model

Figure 6. Histomorphology of corresponding PDX tumor growth in heterotopic and orthotopic model

Figure 7. Comparison of corresponding PDX tissue in heterotopic and orthotopic model with FDG-PET results

Figure 8. Correlation between FDG uptake and glycolysis-related protein levels

PART II. Development of prediction model with a gene signature for FDG avidity in gastric cancer

Table 3. Characteristics of human gastric cancer PDX tissues

Table 4. Primers for gene expression analysis by qRT-PCR

Table 5. Characteristics of the PET-scanned advanced gastric cancer patients

Table 6. Correlation analysis between SUVmax/PETscore and EMT-related *HIF1A* downstream

Figure 9. Study design

Figure 10. Glucose uptake in mouse tumor model bearing gastric cancer PDX tissues

Figure 11. Weighted gene co-expression network analysis of RNA-seq data

Figure 12. Establishment of FDG uptake prediction model for gastric cancer

Figure 13. Validation of the prediction model in human

Figure 14. Molecular characteristic landscape of gastric cancer with PETscore

Figure 15. Association between PETscore and gastric cancer type

Figure 16. Association between PETscore and microsatellite instability

Figure 17. The comprehensive illustration showing the relationship between molecular characteristic landscape and PETscore

Figure 18. Genomic alterations associated with PETscore in gastric cancer

Figure 19. Survival analysis using TCGA and ACRG data

Figure 20. Examples in clinical application with the PETscore

Figure 21. Investigation of FOLFOX sensitivity-related SUVmax and PETscore in human

INTRODUCTION

Gastric cancer (GC) has been characterized by its tumor heterogeneity at molecular, histological and phenotypic levels (1, 2). Accurate diagnosis is essential for cancer treatment. For assessment of the tumor site and lymph node involvement in GC, various medical imaging modalities, such as computerized tomography (CT), Magnetic Resonance Imaging (MRI), endoscopic ultrasound imaging (EUS), and positron emission tomography (PET), are commonly used (3). Unlike other imaging modalities, 2-Deoxy-2-[^{18}F]fluoro-D-glucose ([^{18}F]FDG) PET has been established as a metabolic imaging modality in clinical cancer diagnostics because of the high rate of glucose consumption in cancers, historically being described first by the Warburg-effect (4-7).

Limitations of [^{18}F]FDG-PET in gastric cancer

Clinical utility of [^{18}F]FDG-PET in gastric cancer however remains controversial, especially in respect of the aforementioned tumor heterogeneity. Regarding detecting tumors by [^{18}F]FDG-PET scan in patients with gastric cancer, 40-63% for early gastric cancers (EGC) and 62-98% for advanced gastric cancers (AGC) are identified (8-13). Furthermore, [^{18}F]FDG avidity has been shown to be lower in cancers of the diffuse type with signet ring cells, high mucinous content, and lower cellularity (10, 11,

14). Because of the diversity in characteristics of stomach cancer in terms of the aggressiveness as well as histology and genomic alteration, features highly associated with [^{18}F]FDG avidity have not yet been fully understood.

Patient-derived xenograft models as patient surrogates

In order to improve the clinical utility of [^{18}F]FDG-PET and gain knowledge of the glucose metabolism in GC, appropriate pre-clinical *in-vivo* models are highly desired. Patient-derived xenograft (PDX) models, which are developed by xenograft of human tumors into immune-compromised mice, are useful models for pre-clinical studies (15–16). One of the main advantages of PDX is that PDX tumors recapitulate biological and genetic characteristics of their parental tumors.

Recent high-throughput technologies, which can easily and robustly generate large-scale molecular profiling data, offer extraordinary opportunities to integrate clinical and genetic data into models associated with cancer characteristics. Several studies have demonstrated significant correlation between genetic profiles and the PET parameters for different cancer entities (17–20). In spite of the individual gene level evidence, how the metabolic milieu systematically influences the heterogeneous FDG avidity of GC has not been fully understood. So far, no comprehensive system biologic analysis dealing with the FDG avidity prediction and

association of the molecular-genetic characteristics of GC.

In these regards, human gastric cancer PDX models as patient surrogates are considered useful for the molecular characteristic landscape of GC associated with glucose metabolic profiles non-invasively evaluated by FDG-PET.

Purpose of this study

We hypothesized that [^{18}F]FDG avidity in GC can be predicted by a combination of FDG avidity-associated gene expressions. Therefore, this study aimed to develop a prediction model for FDG avidity in GC by RNA sequencing data paired with [^{18}F]FDG-PET images using PDX murine models. In PART I, we establish appropriate small animal PET imaging protocol for large-scaled preclinical *in-vivo* study. In PART II, we identify a gene signature to develop a prediction model for FDG avidity in GC and investigate its molecular characteristic landscape.

PART I.

**Establishment of protocol for preclinical PET imaging of
human gastric cancer PDX models**

MATERIALS AND METHODS

Establishment of human gastric cancer PDX

Gastric cancer tissues were obtained from patients who underwent gastrectomies at Seoul National University Hospital in 2014 and 2017 with informed consent, and the study was approved by the institutional review board (IRB) of Seoul National University Hospital (No. 1402-054-555) in accordance with the Declaration of Helsinki. Immediately after the tissue acquisition, the samples were transferred to RPMI 1640 medium with 1% penicillin/streptomycin (all from Thermo Fisher Scientific, Waltham, MA, USA).

Establishing gastric cancer PDX models was conducted in collaboration with the Jackson Laboratory. The human tumor tissues were minced into pieces approximately 2 mm in size and subcutaneously injected into the flanks of female NOD.Cg-Prkdc scid Il2rgtm1Wjl/SzJ (NSGTM, 6-week-old) mice (The Jackson Laboratory, Bar Harbor, ME, USA). The tumor volume and body weight of the mice were checked once or twice weekly. The volume was calculated as $(\text{length} \times \text{width}^2)/2$ (21, 22). When tumor volumes reached >700 to 1000 mm³, mice were euthanized and tumor tissues were excised and cryopreserved in liquid nitrogen to generate next passage PDXs. Each successful PDX line was assigned a unique ID (SNU-JAX-GXXX).

Orthotopic and heterotopic PDX model

All procedures involving *in vivo* mouse studies were approved by the Institutional Animal Care and Use Committee (IACUC) at Seoul National University and complied with the Guide for the Care and Use of Laboratory Animals (SNU-170704-3). Female BALB/c nu/nu mice, at age of 6-8 weeks (Orient Bio., Sungnam, Korea) were used to establish mouse tumor models. To minimize the murine stromal contamination in PDX models and losing the patient characteristics (23-25), we used PDX tissues with early passage numbers (P2 or P3).

The orthotopic tumor implantation was performed under general gas anesthesia. The mice were positioned on the right supine position followed by disinfection of the whole abdominothoracic area. A transverse subcostal incision was used to expose the stomach. A first 7-0 non-absorbable mono filament suture was applied seromuscular in longitudinal direction of the corpus of the stomach. This suture was first used as stay suture to expose the stomach during implantation and afterwards to cover the implantation site. The implantation site was chosen in the corpus part of the stomach in the middle of the stay suture, therefore the border to squamous cell epithelium had to be identified safely before. Then a small gastrotomy was performed by micro-scissor, making sure, mucosa is exposed. After one edge of the gastrotomy was caught by another 7-0 suture, the PDX tissue (size approximately 27 mm³) was beaded on the thread and positioned on the gastrotomy. The corresponding edge was sutured and then gently tied over the PDX tissue. It had to

be assured that the PDX tissue connects to the mucosa but would not completely subside in the lumen. Now the longitudinal stay suture was tied over the implantation site in order to completely cover it. Another two 7-0 sutures were applied cranial and caudal to the first one. If a full coverage of the implantation site was achieved, the abdominal cavity was closed by 4-0 absorbable polyfilament suture in two layers, abdominal muscle layer and skin (**Figure 1**). A sham model was performed with similar technique without tumor implantation.

The heterotopic PDX model was performed in standardized way by implanting the tumor tissue via subcutaneous trocar into the right or left flank. For PET imaging, the optimal location of the tumor tissue does not overlap neither with the kidney nor with the heart signal in order to receive a clear signal discrimination. In this case, the tumor is located caudal position of the heart and in cranial position of the ipsilateral kidney.

The clinicopathological features of the donor patients for the PDX tissues used in the orthotopic and heterotopic mouse models are summarized in **Table 1**.

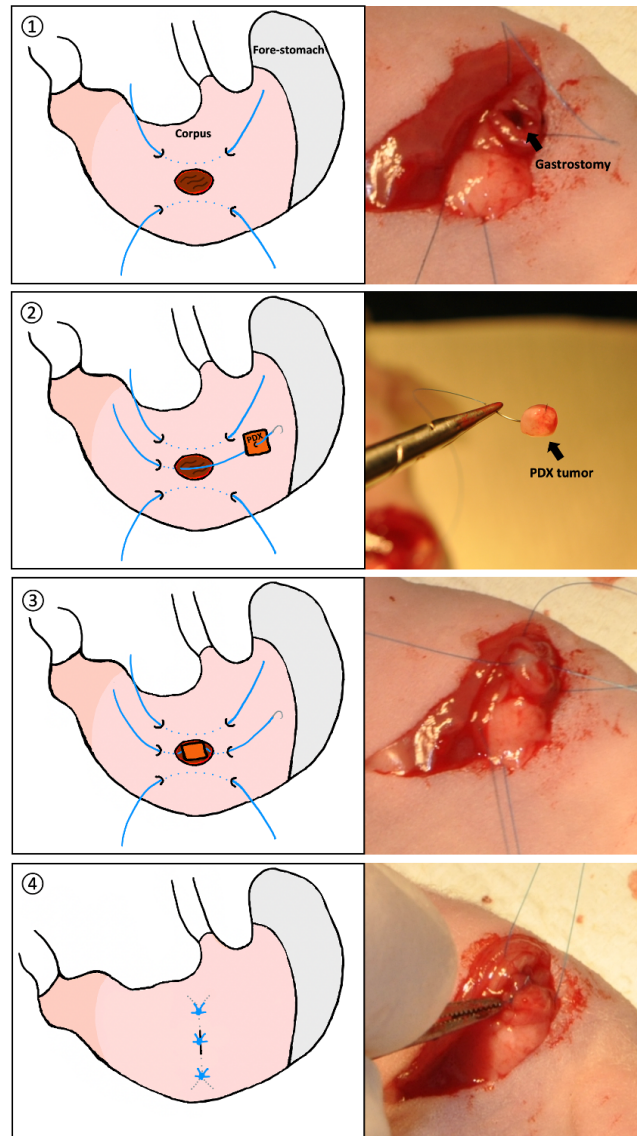


Figure 1. Orthotopic xenograft model of gastric cancer PDX. Schematic illustration of modeling with photographs: ① A small gastrotomy pouch to expose mucosa ② Preparation of PDX tissue ③ Positioning in the gastrotomy pouch ④ Suturing over the tissue.

Table 1. Clinico-pathological characteristics of the donor patients

PDX ID	SNU-JAX-G080	SNU-JAX-G263
Sex	Female	Male
Age	67	56
TNM stage	IIIC	IIb
Lauren classification	Mixed	Diffuse
Histologic type	Others [†]	PD tub [‡]
Gross type	Borrmann 3	EGC-IIc
SUVmax	5.91	3.90

[†]: Mixed carcinoma (mixed tubular adenocarcinoma, moderately differentiated (60%) and poorly cohesive carcinoma (40%))

[‡]: tubular adenocarcinoma, poorly differentiated

Sham-orthotopic model

A sham orthotopic model was performed as control, consisting of the identical procedure as orthotopic tumor implantation, eventually not implanting the tumor. Scanning was performed in intervals and images were evaluated for signal/uptake changes due to inflammation. A longitudinal scanning was also performed for the orthotopic tumor model for the same reason

[¹⁸F]FDG PET/MRI imaging

The mice were starved for 12 to 16 hours and were subsequently anesthetized with 2% isoflurane before [¹⁸F]FDG injection. The body temperature was kept within normal range throughout the whole procedure (26).

Animals were scanned for simultaneous PET/MR imaging using the SimPET simultaneous PET/MRI scanner (Aspect imaging, Israel) (27). [¹⁸F]FDG was intravenously injected into the tail vein with an uptake time of 1 hour. Urinary bladder was evacuated before imaging in order to reduce artefacts.

The final imaging protocol was used as follows: Simultaneous PET/MR scans were acquired for 30 min acquisition time. MR imaging protocol was consisted of T2-weighted fast spin echo sequences with repetition time 3,070 msec and echo time of 63.8 msec. Acquired PET images were reconstructed with 3D OSEM (ordered subset expectation maximization) algorithm.

Acquired PET and MR images were spatially registered for the FDG SUV (standard uptake value) evaluation in the

tumor sites.

To determine adequate [^{18}F]FDG dose, longitudinal PET/MRI imaging at different intervals after [^{18}F]FDG injection was carried out. Four mice bearing heterotopic tumors were injected with higher [^{18}F]FDG dose ($545 \pm 5.6 \mu\text{Ci}$). First image was taken one hour after injection, then three hours and five hours after injection. The corresponding [^{18}F]FDG dose was calculated in respect of the half-life of F-18 of 109.8 minutes (28).

Image Analysis and statistical analysis

The PET/MRI images were converted into Digital Imaging and Communications in Medicine (DICOM) files and analyzed with OsiriX MD (FDA certified; Pixmeo, Bernex, Switzerland). The maximal standardized uptake value (SUVmax) was measured by volume of interests (VOIs).

Spatial resolution of the SimPET with warmed background is 1.45 mm. To minimize the PET signal loss by the partial volume effect, tumors with above 5mm width were scanned. The VOIs were drawn based on the MRI images and measurement of tumor glucose metabolism was derived in PET images. The FDG retention was also quantified in muscles of hind legs and liver tissue in order to illustrate changes over time and correlate with tumor signal.

The statistical analysis and figure calculation were performed using GraphPad Prism (GraphPad Software 8.1.2, San Diego, CA) and a P -value < 0.05 was considered

statistically significant. Results for SUVmax were presented as the mean values with standard deviation. The Mann-Whitney U test for the consecutive imaging and the PET images in the comparison between orthotopic and heterotopic models was conducted to measure *P*-value.

Histology and Immunohistochemistry

After imaging, mice were sacrificed and macroscopically investigated for cancer metastasis. The primary tumor was excised, fixed in 10% formalin solution and consecutively paraffin embedded. Histological confirmation of tumor was performed by an expert pathologist (WHK) on 4 μ m Hematoxylin & Eosin (H&E) stained slides. For immunohistochemistry staining, 4 μ m slides were stained with Glucose transporter 1 antibody (GLUT1, ab115730, Abcam, Cambridge, UK) which is corresponding to Human Glucose Transporter GLUT1 aa 450 to the C-terminus and Hexokinase 2 antibody (HK2, MA5-14849, Thermo Fisher Scientific, MA, USA) which is corresponding to the sequence of human. The staining was performed with Bond-Max Immunostainer and BondPolymer Refine Detection Kit (Leica Microsystems, Germany) according to the manufacturer's instructions.

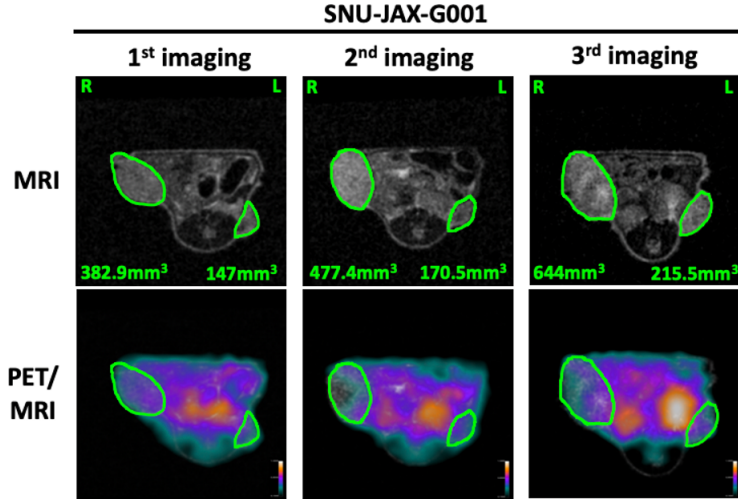
Assessment of immunohistochemistry was performed by application of H-score combining the intensity and degree of staining in the tumor tissue (29).

RESULTS

Selection of optimal tumor size and dose for [^{18}F]FDG PET imaging protocol

Serial imaging of [^{18}F]FDG PET/MRI with injection dose of $449 \pm 33.3 \mu\text{Ci}$ using a heterotopic model showed comparable FDG uptake in tumors and revealed a tumor size of more than 400 mm^3 comes along with central necrosis of the tumor that affects the global uptake of the tumor tissue (**Figure 2A, B**). Consecutive imaging of heterotopic model with primary injection of $545 \pm 5.6 \mu\text{Ci}$ after one, three and five hours resulted in distinctive signal of tumor, liver and muscle in SNU-JAX-G080 (**Figure 3A, B**). The difference of tumor signal, muscle and liver was shown to be stable over time, resulting in satisfactory results after five hours with an approximate obtained [^{18}F]FDG dose of $100 \mu\text{Ci}$. No benefits were seen for higher dose. In respect of the standard uptake time of one hour after injection, a primary injection dose of $150 \mu\text{Ci}$ was expected to result in stable results and was therefore chosen for the protocol (**Figure 4**).

A



B

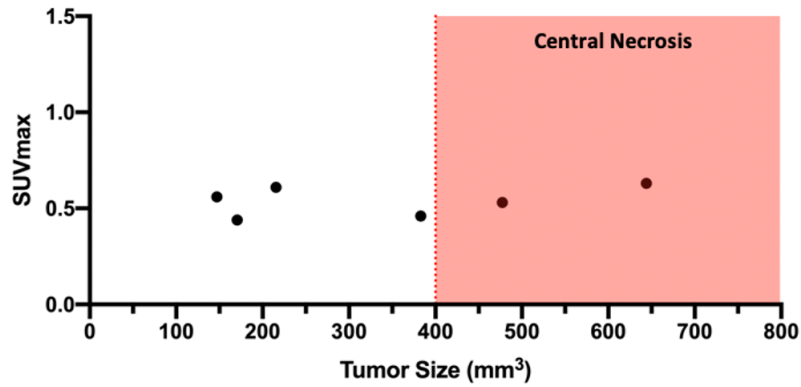
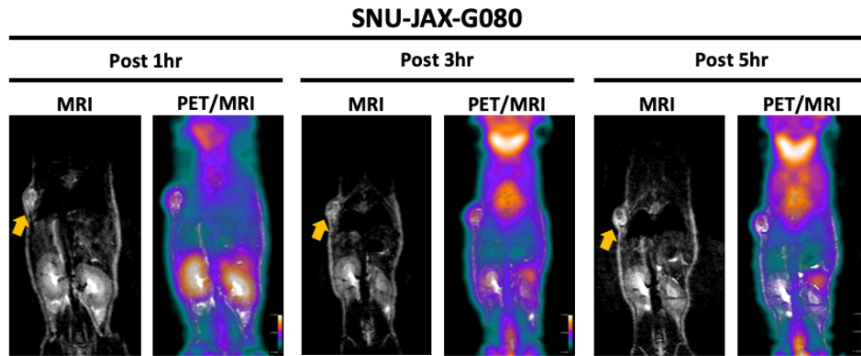


Figure 2. Selection of optimal tumor size for [¹⁸F]FDG PET imaging protocol. (A) Serial PET/MRI images in a heterotopic model at 54 (1st imaging), 61 (2nd imaging), and 72 (3rd imaging) days after modeling. The green ellipsoid indicates a tumor. (B) Evaluation of [¹⁸F]FDG uptake in different size tumors.

A



B

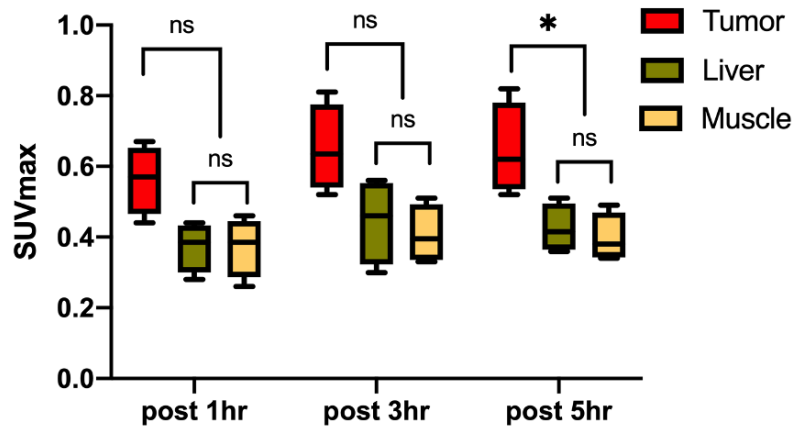


Figure 3. Selection of optimal dose for [^{18}F]FDG PET imaging protocol. (A) Consecutive PET/MRI images of mice-bearing heterotopic PDX tumor at 1, 3, and 5 hours following injection of [^{18}F]FDG (n = 4). The yellow arrow indicates a tumor. (B) [^{18}F]FDG uptake measurements in tumors and in normal background tissues. Box plots with error bars indicate the mean uptake and the standard deviation across the mice.

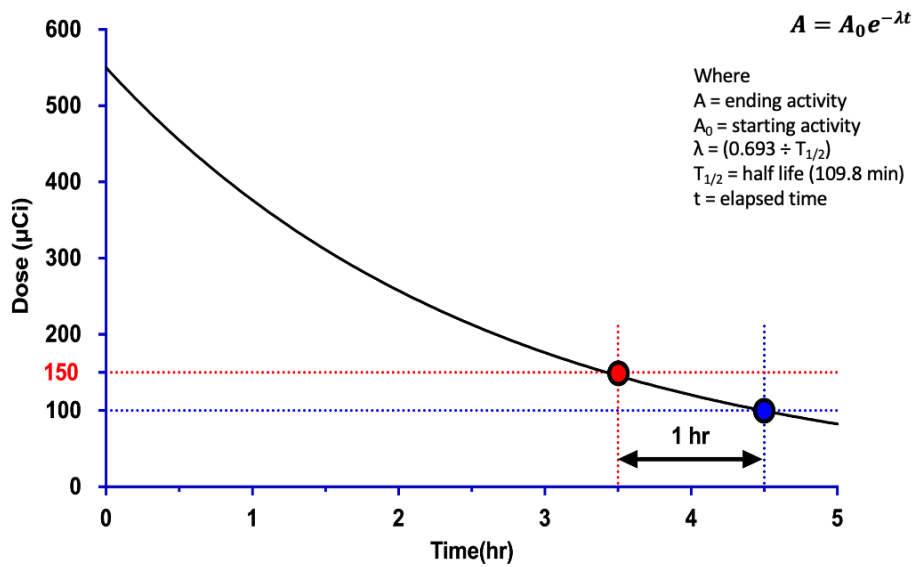
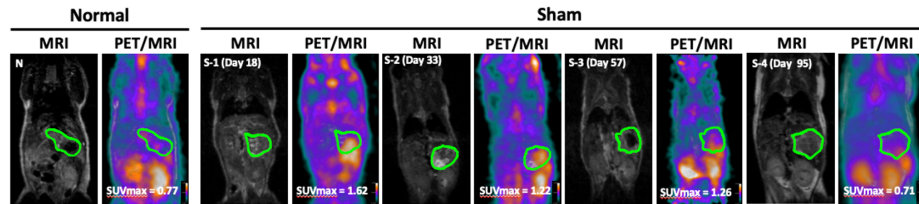


Figure 4. Injection dose selection for PET imaging protocol from the theoretical decay curve of F-18. The ideal half life of F-18 is 109.8 minutes. Considered the decay time, a primary injection dose of 150 μCi is expected to reach about 100 μCi in the mouse body.

Inflammatory signal aspect for orthotopic model

The sham model underwent FDG PET/MRI scanning at Day 18, 33, 57, and 95 after sham implantation. FDG uptake analysis revealed that the SUVmax value decreased from 1.62 at Day 18 to 0.71 at Day 95 in the same intervals. (**Figure 5**). Two mice without any manipulation at any site (“healthy control”) showed a stomach site with SUVmax of 0.77 and 0.54. The Day 95 sham model showed comparable SUVmax (0.71) compared with the control mice (SUVmax = 0.66 ± 0.16).

A



B

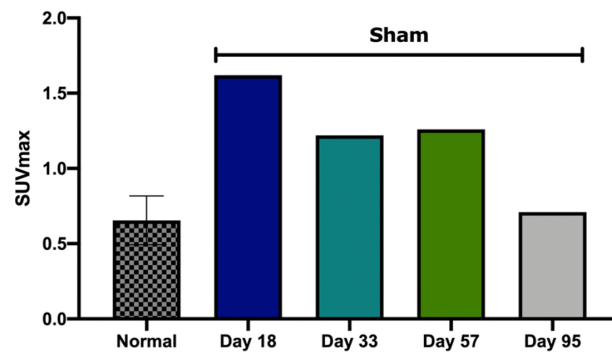


Figure 5. Inflammatory PET signal aspect for orthotopic model. (A) [^{18}F]FDG PET/MRI images of normal (n = 2) and sham mouse models. The green ellipsoid indicates a stomach. (B) Quantitative analysis of FDG uptake using SUVmax in stomach.

Comparison of corresponding PDX tissues in heterotopic and orthotopic model

Six mice were used for heterotopic models with subcutaneously implanted two different PDX tissues. Eight mice were orthotopically implanted with the same PDX tissues. Two mice deceased before scanning. All (100%) heterotopic and seven mice (87.5%) of the orthotopic models presented histologically proven cancer growth under microscopic investigation. The histo-morphology of heterotopic and orthotopic PDX models are demonstrated in **Figure 6 and Table 2**.

The remaining orthotopic mice were scanned after a mean time of 95 days after implantation. All heterotopically implanted mice underwent FDG-PET/MRI with a mean tumor size of 134.9 mm² after a mean time of 39 days. The [¹⁸F]FDG avidity of orthotopic and heterotopic PDX models with identical tissues is demonstrated in **Figure 7A, B**. Results suggest a higher avidity of tumor in orthotopic environment as in those cases the mean SUVmax was measured with 0.8 and 0.7 in SNU-JAX-G080 and SNU-JAX-G263 in heterotopic and 1.3 and 1.2 in orthotopic models. The orthotopic tumor growth could be clearly distinguished in MRI.

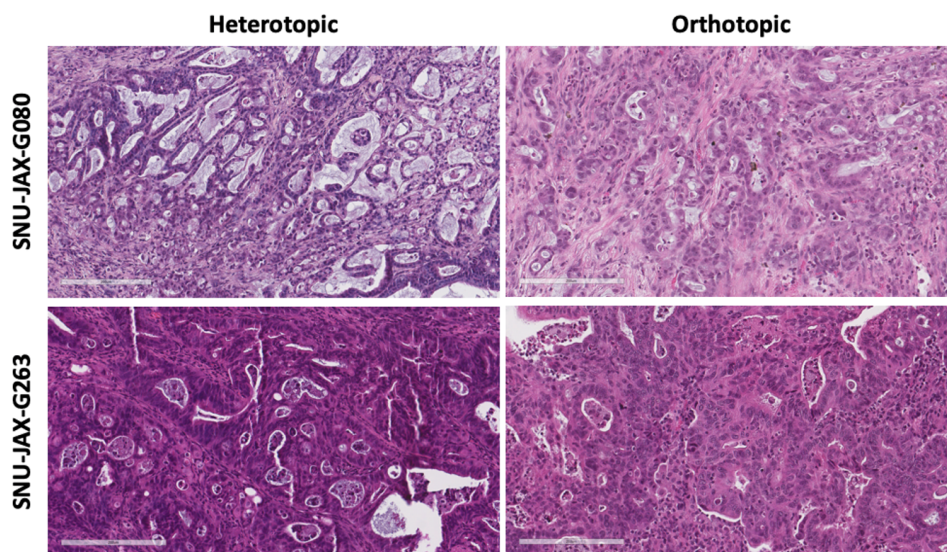
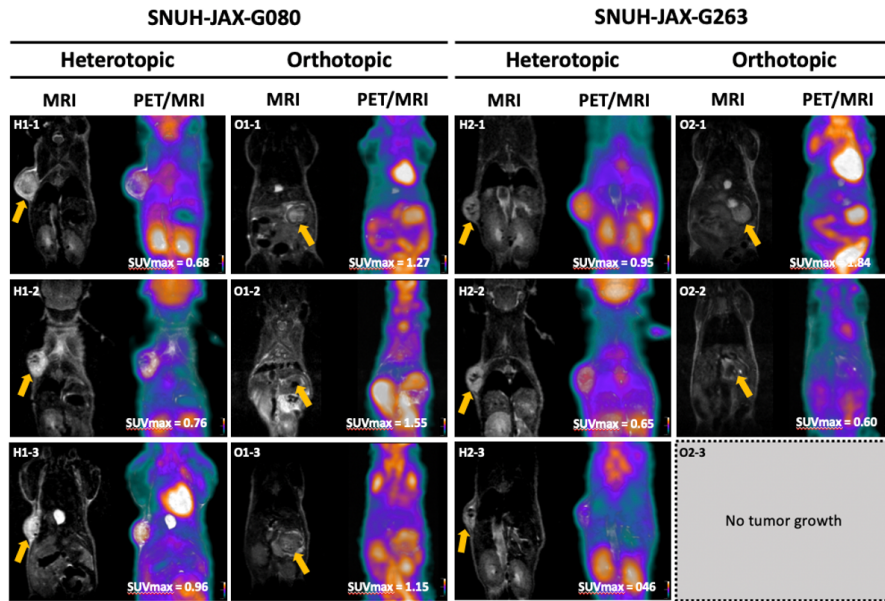


Figure 6. Histomorphology of corresponding PDX tumor growth in heterotopic and orthotopic model. Representative hematoxylin-eosin staining (H&E) images of tumor growth in established models (Magnitude with X200).

Table 2. Summary of successful rate between heterotopic and orthotopic models

	Heterotopic	Orthotopic
Total used mice	6	8
SNU-JAX-G080 (Passage No.)	3 (P2)	4 (P2)
Tumor growth	3/3 (100%)	4/4 (100%)
Decease	0/3 (0%)	1/4 (25%)
SNU-JAX-G263 (Passage No.)	3 (P2)	4 (P2)
Tumor growth	3/3 (100%)	3/4 (75%)
Decease	0/3 (0%)	1/4 (25%)
Model successful rate	6/6 (100%)	7/8 (87.5%)

A



B

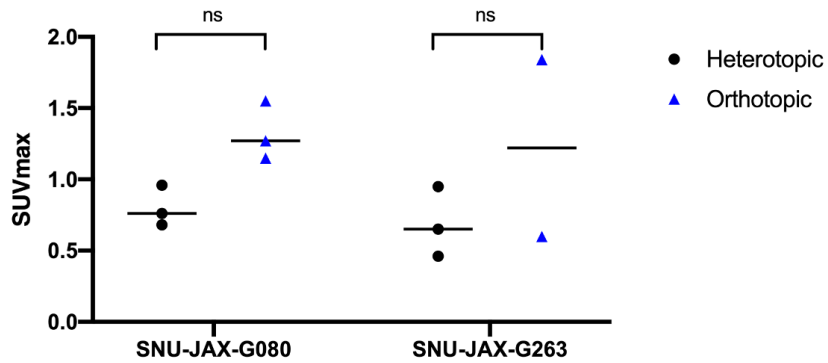
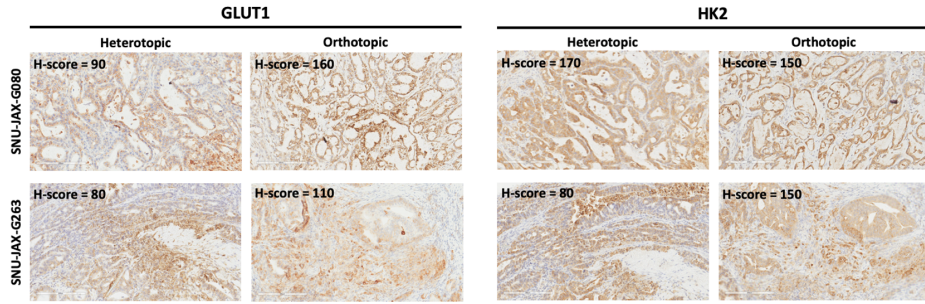


Figure 7. Comparison of corresponding PDX tissue in heterotopic and orthotopic model with FDG-PET results. (A) ^{18}F FDG PET/MRI images of heterotopic and orthotopic mouse models. (B) Quantitative analysis of uptake using SUVmax of ^{18}F FDG in heterotopic and orthotopic models-bearing PDX tumor.

Expression levels of GLUT1 and HK2 in PET-scanned tumors

Orthotopic cases showed higher expression of both, GLUT1 and HK2 corresponding to higher SUV max in orthotopic cases. Comparing all cases, the model with the highest SUVmax (1.3, SNU-JAX-G080, orthotopic) showed the highest scores for GLUT1 (177) and HK2 (170). The case with the lowest SUV max (0.69, SNU-JAX-G263, heterotopic) showed the lowest scores for GLUT1 (57) and HK2 (73). Comparison between SUVmax and each marker showed significant positive correlation (GLUT1: Pearson $r = 0.7429$, P -value = 0.0088, HK2: Pearson $r = 0.6048$, P -value = 0.0487). Results of GLUT1 and HK2 immunohistochemistry are shown in **Figure 8**.

A



B

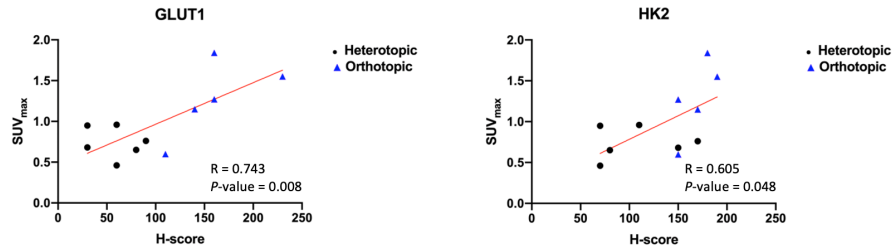


Figure 8. Correlation between FDG uptake and glycolysis-related protein levels. (A) Representative immunohistochemistry results of GLUT1 and HK2 in PET-scanned tumors (IHC stain, X200). (B) Comparative analysis between SUVmax and immunohistochemical staining score (Pearson $r = 0.743$, P -value < 0.01 for GLUT1, Pearson $r = 0.605$, P -value < 0.05 for HK2).

PART II.

**Development of prediction model with a gene signature for
FDG avidity in gastric cancer**

MATERIALS AND METHODS

Study design

This study was an observational proof-of-concept study using gene expression and FDG-PET image data. We developed a model for predicting [^{18}F]FDG-avid gastric cancer using patient-derived xenograft (PDX) models, and clinical applicability of the model was evaluated by RNA sequencing (RNA-seq) and real-time reverse transcription PCR (qRT-PCR) in gastric cancer patients. The study design and flow process are depicted in **Figure 9**.

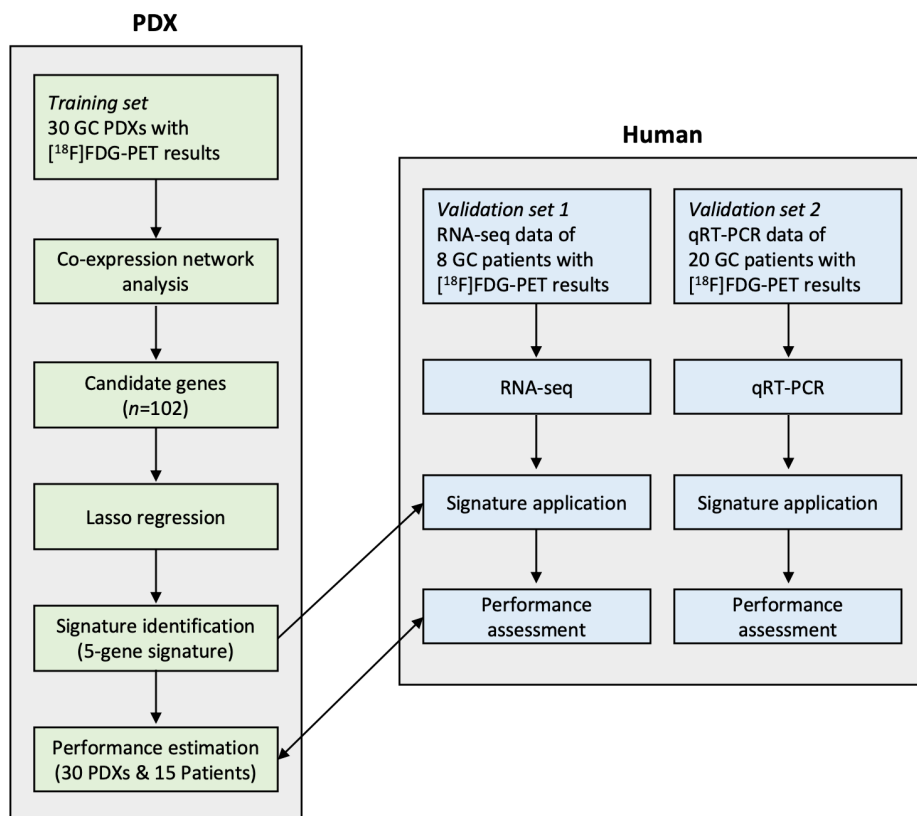


Figure 9. Study design. FDG-avidity prediction model is established investigating the gene expression profiles of thirty gastric cancer PDXs with [^{18}F]FDG-PET images. The model is then evaluated in human by RNA-seq and qRT-PCR with the gene signature.

Human [¹⁸F]FDG-PET imaging and analysis

PET imaging of patients was collected. According to the standard protocol of our hospital, patients were injected intravenously 5.18 MBq/kg of FDG after fasting for at least 6 hours with blood glucose level < 140 mg/kg. PET/CT scans were started 60 minutes after injection, using dedicated PET/CT scanners or a PET/MR scanner (Biograph 40, mCT, and mMR, Siemens). An emission scan was acquired from the skull base to the proximal thigh. A CT scan was also obtained for attenuation correction. For PET/MR, attenuation correction map was generated by DIXON sequence. PET images were reconstructed using an iterative algorithm (ordered-subset expectation maximization).

All PET images were reviewed by the experienced nuclear medicine physician using commercial imaging software (Syngo.via, VA 30; Siemens Healthcare, Erlangen, Germany). To evaluate FDG uptake of tumors, spherical volume of interests (VOIs) were drawn for each patient. In each VOI, the maximum standardized uptake value (SUVmax) was measured.

Nude mouse tumor modeling with 30 PDX cases

Thirty PDX cases for the present study were available among the established PDXs. Six-week-old female BALB/c nu/nu mice (Orient Bio., Sungnam, Korea) were used to establish mouse tumor models ($n = 3$ per PDX case). The mouse tumor modeling was performed by subcutaneous

implantation using a trocar as previously described (30).

All procedures involving in vivo mouse studies were approved by the Institutional Animal Care and Use Committee (IACUC) at Seoul National University and complied with the Guide for the Care and Use of Laboratory Animals (IACUC No. SNU-170704-3). Overall characteristics of GC PDXs are summarized in **Table 3**.

Table 3. Characteristics of human gastric cancer PDX tissues

Variable	<i>N</i> (%)
Total no. of PDX cases	30
Lauren classification	
Intestinal	10 (33.3%)
Diffuse	9 (30%)
Mixed	9 (30%)
Undetermined	2 (6.7%)
WHO classification	
Well Differentiated tubular adenocarcinoma	1 (3.3%)
Moderately Differentiated tubular adenocarcinoma	6 (20%)
Poorly Differentiated tubular adenocarcinoma	14 (46.7%)
Signet-Ring Cell carcinoma	4 (13.3%)
Others	4 (13.3%)
Unknown	1 (3.3%)

Small animal [^{18}F]FDG-PET imaging and analysis

Small animal [^{18}F]FDG-PET/MRI imaging was performed as previously described (1). After fasting for at least 12 hours, mice were subsequently anesthetized with 2% isoflurane before [^{18}F]FDG injection. The mice were scanned by simultaneous μ PET/MRI scanner for small animal (Brightonix, Seoul, Korea). [^{18}F]FDG was intravenously injected in tail vein with an uptake time of 1 hour. Urinary bladder was evacuated before imaging in order to reduce artefacts. Simultaneous PET/MRI scans were acquired for 30 min acquisition time.

The micro PET/MRI images were converted into Digital Imaging and Communications in Medicine (DICOM) files and analyzed with OsiriX MD (FDA certified; Pixmeo, Bernex, Switzerland). SUVmax was measured by VOIs. Acquired PET and MRI images were spatially registered for SUVmax evaluation in the tumor sites. The VOIs were drawn based on the MRI images and measurement of tumor glucose metabolism was derived in PET images.

RNA sequencing and data preprocessing

For acquisition of the RNA-seq data, RNA from the PDX or human tissues was extracted using TRIzolTM (Invitrogen, Waltham, MA, USA.). Samples with RNA integrity number (RIN) of greater than 5 were further processed. The 101 bp paired-end libraries were constructed with the TruSeq RNA Sample Prep Kit v2 (Illumina) using 1 μg of RNA. Whole transcriptome sequencing (WTS) was performed on

Illumina HiSeq 2000 instruments.

Sequenced read counts of PDXs were aligned to combined human and mouse reference with STAR (2.4.1d). Duplicate reads were removed with Picard(1.1.34). HTSeq-count (0.6.1) was used to calculate read counts.

WGCNA analysis

We used Weighted Gene Co-expression Network Analysis (WGCNA) package (31) to identify gene network modules from the 30 PET-scanned PDXs (training set). We created a correlation matrix on the basis of the Pearson's correlation coefficient for all pair-wise genes across all samples. The power—the key parameter for the weighted network—was selected to optimize both scale-free topology and sufficient node connectivity and we chose a threshold of 10 in this study. The correlation matrix was transformed into an adjacency matrix (matrix of connection strength) using the power function, and pair-wise topological overlap between genes was calculated.

Development of FDG avidity prediction model

We used *glmnet* R package (32) to identify the most significant gene signature related with SUVmax.

The proposed the [¹⁸F]FDG-avid tumor prediction model using the least absolute shrinkage and selection operator (Lasso) regression can be written as follows:

$$Y'_i = \sum_{j=1}^p X_{ij}\beta_j + \beta_0$$

via minimizing $\sum_{i=1}^n (Y_i - Y'_i)^2 + \lambda \sum_{j=1}^p |\beta_j|$

where the Y is actual SUVmax, the Y' is predictive SUVmax in PDX (PETscore) and the X_{ij} is RNA-seq read count for each gene. The n is the total number of PDX cases, the p is the total number of genes in the module. The β is the regression coefficient of each variable, which indicates how each gene explains the gene signature. The λ is a factor that determines the sparsity of the solution; as λ increases, the number of non-zero components of β decreases. To optimize λ , we tried many values of λ and used those that minimize the mean square error. The penalty regularization parameter λ was determined via the cross validation routine *cv.glmnet* function (10-fold cross validation). The value was finalized by using *lambda.1se*, which gives the most regularized model such that error is within one standard error of the minimum. The performance of the prediction model was assessed using RNA-seq data of 15 patients who underwent FDG-PET in the training set.

Human tissue specimens for the prediction model validation

PET results and RNA-seq data of eight GC patients were available for the model validation. Twenty fresh frozen tissues among GC patients who underwent FDG-PET scan were available for additional validation by qRT-PCR. All tissue samples were obtained from Seoul National University Hospital, Korea, and written informed consent was obtained from all patients. The present retrospective validation was approved by the IRB of Seoul National

University Hospital (IRB No. 1910-045-1069).

qRT-PCR analysis

Total RNA was isolated from frozen tissue samples using the Trizol reagent. cDNA was synthesized to analyze mRNA expressions using a TOP script cDNA synthesis kit (Enzynomics, Daejeon, Korea) according to the manufacturer's protocols. The expression levels of the five genes (*PYY*, *SLC6A5*, *HBQ1*, *PLS1*, *NAT16*) were measured using SYBR Green Master Mix (Applied Biosystems, Carlsbad, CA) by normalizing to the levels of GAPDH. Primer sequences are described in **Table 4**. The reaction was performed and analyzed by comparative ΔC_t methods (33) using Step One Plus Real-Time PCR system (Applied Biosystems, Carlsbad, USA).

Normalization and regularization of the qRT-PCR results for applying the PETscore based on results using RNA-seq data. Each gene expression level ($-\Delta C_T$) was normalized by standard deviation: $X - \text{median}(X) / SD(X)$ and then transformed into z-score for each tissue sample. Here X is each gene expression level for samples and SD indicates the standard deviation. Based on the rationale from the results of the Lasso modeling, four genes (*PYY*, *SLC6A5*, *HBQ1*, *PLS1*) had positive weighted values one gene (*NAT16*) had negative one, PETscore with qRT-PCR data can be written as follows: $PETscore = (\text{sum of positive gene levels}) - (\text{negative gene level})$. The PETscore was then applied to the FDG uptake results to confirm the correlation.

Table 4. Primers for gene expression analysis by qRT-PCR

Gene	Amplicon Size		Sequence (5' -> 3')	Length	Tm
PLS1	100	Forward	TGGCGGCAGATATAAGACCT	21	61.55
		Reverse	GCCTCTTGAGTTCTTCAAGCTC	23	61.68
SLC6A5	101	Forward	TTACATGTTTCAGCTTGTGGAC	22	59.62
		Reverse	CTTTGCAAGCCATACACATAAGAG	24	60.72
NAT16	105	Forward	CCGAGCCATTGGACTTCGT	19	62
		Reverse	GGTAGCGGCTAGGAAGGTAGT	21	62.5
HBQ1	106	Forward	TCCTGAGGCCACGTTATCTCG	20	61.87
		Reverse	GGAGAGGCTTTACTCAAACACG	22	61.69
PYV	139	Forward	AAGAACTGACTCAGGTCAATTGGT	22	59.87
		Reverse	AGGCAAACTCCTTATCTTAGCT	22	59.4

Acquisition of TCGA data

Genome and transcriptome data of stomach cancer of TCGA projects were used. For transcriptome data, TCGABiolinks R package was used for downloading from TCGA data portal (<https://portal.gdc.cancer.gov/>) (34). The transcriptome data of TCGA-STAD were normalized by “TCGAAnalyze_Normalization” function.

Genomic alterations of the STAD were downloaded from <https://github.com/PoisonAlien/TCGAmutations>. Mutation data were curated and analyzed by maftools package (35). Clinical data of stomach cancer (TCGA-STAD) were downloaded from cBioPortal (<https://www.cbioportal.org>).

Metabolic profiles of TCGA data

Metabolic profiles of TCGA-STAD data were estimated by transcriptome data. Single sample gene set enrichment analysis (ssGSEA) was used to calculate enrichment scores of metabolic profiles (36). RNA-seq data were changed to counts per million reads (CPM) and then curated genes according to predefined gene sets of MSigDB2 (37). GSVA package was used to apply ssGSEA to each transcriptome data. The enrichment scores of metabolic pathways were normalized by Z-score.

Acquisition of ACRG data

Clinical and Microarray datasets (GSE62254, n=300) were downloaded from the Gene Expression Omnibus (GEO) database (<http://www.ncbi.nlm.nih.gov/geo/>). The samples with Lauren and molecular subtypes were filtered by the

calculated PETscore of the transcriptome data or overall survival results.

FOLFOX response evaluation

Drug treatments began after the tumors reached approximately 200 mm³. Mice were divided randomly into control and FOLFOX treated groups, with five mice in each group. 5-FU (Selleckchem, 5 mg/kg, weekly) and Oxaliplatin (Selleckchem, 50 mg/kg, weekly) in saline was administered via intraperitoneal injection for 21 days. The volume of the tumors was checked three times weekly and was calculated as $(\text{length} \times \text{width}^2) / 2$. The tumor volume ratio between the treatment and the vehicle group was calculated as the division of the average tumor volume of each group at the final measurement ($V_{\text{Treat}} / V_{\text{Vehicle}}$). The final tumor volume ratio and p-value of analysis of variance (ANOVA) test reflecting the trend of tumor growth was used for the evaluation of antitumor efficacy. ANOVA test was performed using SPSS program. The tumor volume ratio less than 0.5 and the ANOVA *P*-value < 0.001 was defined as the responder. Non-responder was defined as *P*-value > 0.05. Others were defined as moderate responder.

Statistical analysis

The Spearman's correlation analysis was performed

between the predicted SUVmax and the actual SUVmax using *ggplot2* R package (38). Correlation coefficients and *P*-values were gained and used to sort statistically significant features (*P*-value < 0.05). All statistical analyses were performed in R (version 3.5.3).

The linear models for microarray data (*limma*) package (39) in R (x64, version 3.5.3) was utilized to identify genes associated with SUVmax. False discovery rate (FDR) < 0.05 was used for selecting the genes associated with SUVmax.

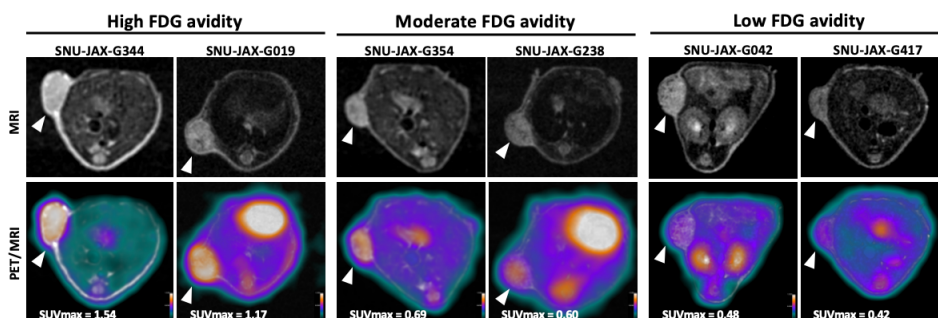
The statistical analysis (Mann-Whitney U test) and figure calculation of comparison between SUVmax and individual gene expression were performed using GraphPad Prism (GraphPad Software 8.1.2, San Diego, CA).

RESULTS

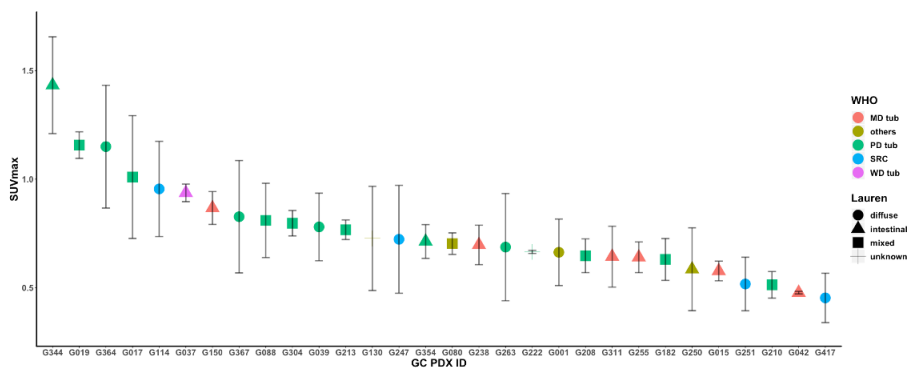
Measurement of [^{18}F]FDG uptake in mouse tumor model bearing GC PDXs.

To evaluate FDG avidity in different PDX cases with a PET/MRI scanner, 30 PDX cases were used. The median SUVmax of the 30 PDX cases was 0.708 (range, 0.453–1.433). Representative images and FDG uptake measurement in tumor of PDX cases are shown in **Figure 10A, B**. The SUVmax of PDX cases were significantly correlated with SUVmax of their parental tumors ($n = 15$, Spearman $r = 0.54$, P -value = 0.04, in **Figure 10C**).

A



B



C

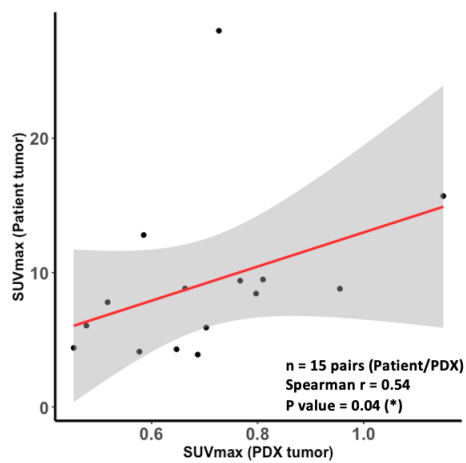
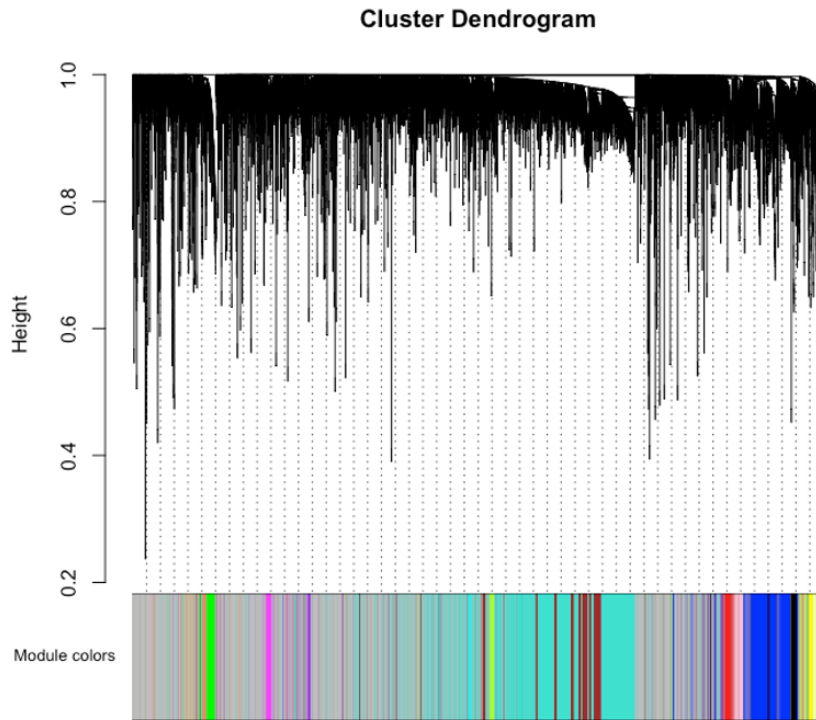


Figure 10. Glucose uptake in mouse tumor model bearing gastric cancer PDX tissues. (A) Representative [^{18}F]FDG-PET/MRI images (B) Quantitative analysis of PET images of PDX tumors. (C) Correlation between parental tumors and corresponding PDXs. The gray shading around the line represents a confidence interval of 0.95.

Weighted gene co-expression network analysis of 30 GC PDX RNA-seq data

WGCNA was performed on the preprocessed 16,927 genes of 30 PDX samples. We identified network modules using a hierarchical clustering method with topological overlap dissimilarity as the distance measure. The modules were detected by the dynamic tree cut algorithm in WGCNA package, defining a height cutoff value of 0.99, deep split as 4, and minimum module size cutoff value of 40. Genes that were not assigned to any module were classified to color gray (**Figure 11A**). Nineteen co-expression network modules that contained groups of genes with similar patterns of connection strengths with other genes were identified (**Figure 11B**). The highest association was found between the midnightblue module and SUVmax ($r = -0.92$, $P\text{-value} = 1.8e-42$) by Pearson's correlation analysis. This module containing 102 genes associated with SUVmax had the highest significance across all modules. The module was selected for subsequence analysis steps.

A



B

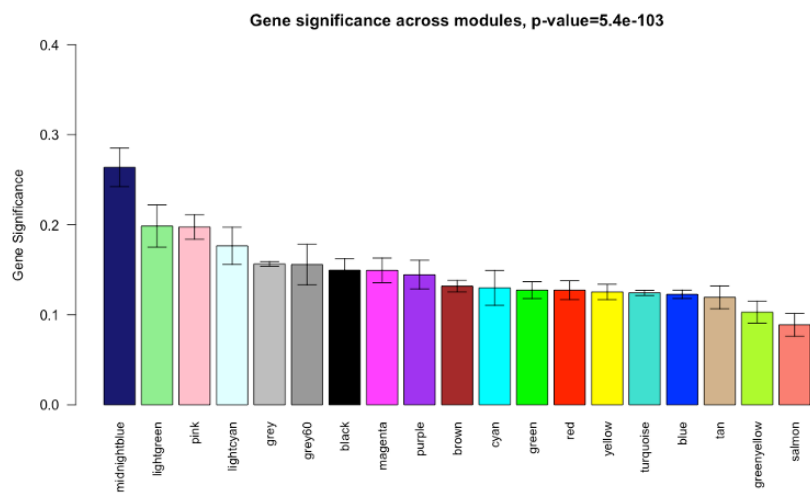


Figure 11. Weighted gene co-expression network analysis of RNA-seq data. (A) Cluster dendrogram and module assignment for modules from WGCNA. The branches correspond to modules of highly inter-connected gene sets. Colors in the horizontal bar represent the modules. (B) Bar plot of average gene significance across all genes in each module.

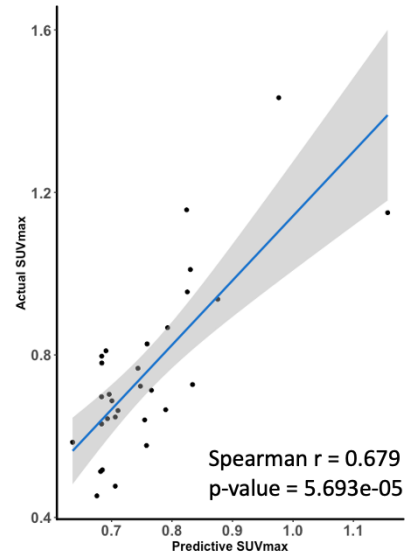
Establishment of [¹⁸F]FDG uptake prediction model: PETscore

Based on the result of WGCNA, we used a Lasso logistic regression (Lasso) combined with 10-fold cross validation to build a predictor for SUVmax in the 30 PDX cases. The Lasso provided a gene signature with five genes (*PLS1*, *SLC6A5*, *NAT16*, *HBQ1*, *PYY*) as the best predictor of SUVmax in the 30 PDX training set. A prediction formula with the gene signature was derived to calculate SUVmax for each PET-scanned PDX and showed a significantly positive correlation (Spearman $r = 0.679$, P -value = $5.693e-05$) between predicted SUVmax and actual SUVmax (**Figure 12A**). We developed a scoring system (*PETscore*) based on the five gene expression levels for application in human. For estimation of the model performance in human, we applied the PETscore to 15 PET-scanned patients who were paired with the 15 PDXs in the training set. The SUVmax of these 15 patients were significantly correlated with the PETscore estimated by RNA-seq of the parental tumor (Spearman $r = 0.557$, P -value = 0.034) (**Figure 12B**).

A

$$Y'_i = \sum_{j=1}^p X_{ij}\beta_j + \beta_0$$

	features	Coefficient
β_0	Intercept	0.7583333333
	PYY	0.0423299531
	PLS1	0.0003261771
β_j	HBQ1	0.0707276627
	SLC6A5	0.0338267003
	NAT16	-0.0288354457



B

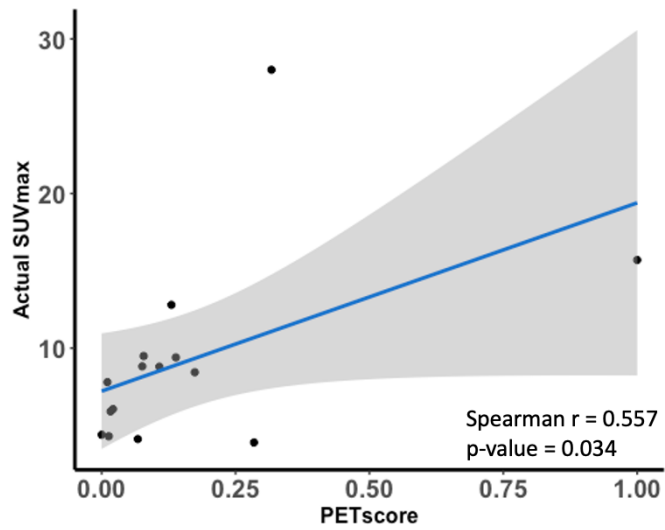


Figure 12. Establishment of FDG uptake prediction model for gastric cancer. (A) The prediction model based on expression levels of the five genes. The formula provides significantly positive correlation between actual SUVmax and predicted SUVmax in PDXs (Spearman $r = 0.679$, P -value = $5.693e-05$). (B) PETscore calculated based on the formula in 15 PET-scanned patients shows a positive correlation with actual SUVmax (Spearman $r = 0.557$, P -value = 0.034). The gray shading around the line represents a confidence interval of 0.95.

Validation by RNA-seq and qRT-PCR in human

To validate the prediction model in an independent cohort, we applied the model to 28 PET-scanned patients. Eight patients among 28 patients were available to use RNA-seq data and 20 patients were assessed with the expression of the five genes (*PYY*, *SLC6A5*, *HBQ1*, *PLS1*, *NAT16*) by qRT-PCR method. The representative PET images are depicted in **Figure 13A**. The clinicopathological features of the 28 patients with GC are summarized in **Table 5**.

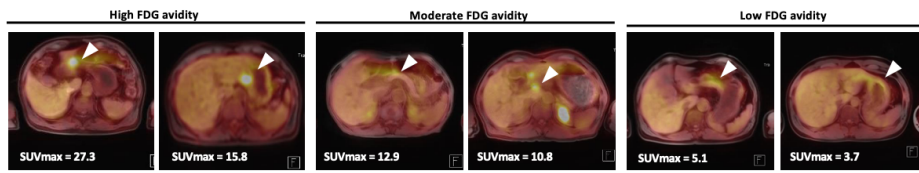
The prediction performed on 8 PET-scanned patients showed significant correlation with actual SUVmax of the 8 patients (Spearman $r = 0.905$, P -value = 0.005) (**Figure 13B**). To apply the model based on RNA-seq data to qRT-PCR results, the gene expression values were regularized and transformed to z -score to assign comparable weights. After that, PETscore which is a combination of qRT-PCR results was utilized to validate the performance of the five predictors for FDG uptake in gastric cancer. The PETscore showed significant correlation (Spearman $r = 0.464$, P -value = 0.039) with SUVmax in 20 patients (**Figure 13C**).

Table 5. Characteristics of the PET-scanned advanced gastric cancer patients

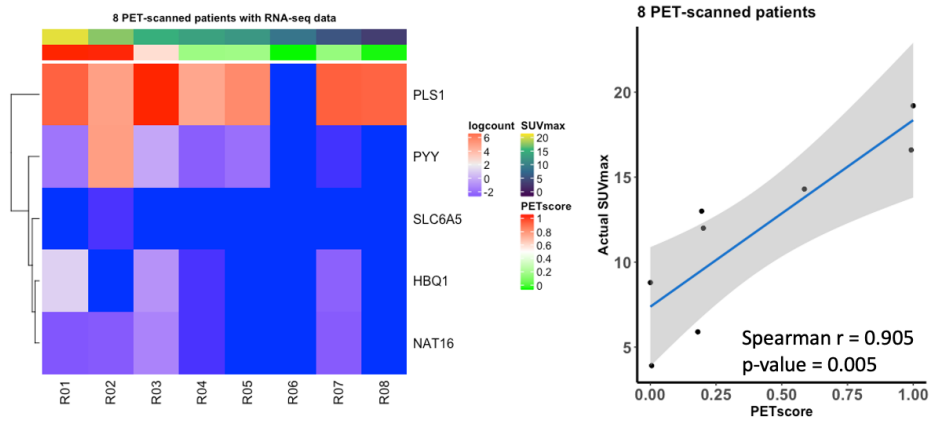
Variable	RNA-seq validation	qRT-PCR validation
Total no. of patients	<i>N</i> = 8	<i>N</i> = 20
Sex		
Male	6	16
Female	2	4
Age, years		
Median (range)	60.5 (46-78)	70 (31-88)
SUVmax		
Median (range)	12.5 (3.91-19.2)	9.6 (3.7-27.3)
TNM stage		
IIa	-	4
IIb	-	2
IIIa	-	2
IIIb	1	7
IIIc	5	1
IV	2	4
Borrmann type*		
I	1	3
II	-	4
III	7	8
IV	-	3
Unknown	-	1
Lauren classification*		
Intestinal	4	10
Diffuse	3	8
Mixed	-	1
Unknown	1	-

* One patient is palliative gastro-jejunostomy bypass case in qRT-PCR validation group.

A



B



C

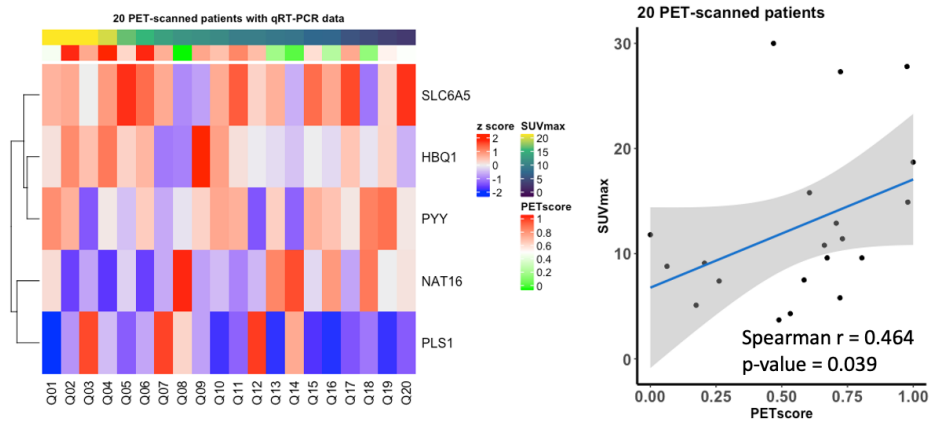


Figure 13. Validation of the prediction model in human. (A) Representative [^{18}F]FDG PET/MRI images of 28 PET-scanned gastric cancer patients. (B), (C) Heatmap displaying the z-scores of the expression levels on the five genes measured by RNA-seq and qRT-PCR. (C) Correlation between SUVmax and results by each validation method shows significantly positive (RNA-seq: Spearman $r = 0.905$, P -value = 0.005, qRT-PCR: Spearman $r = 0.464$, P -value = 0.039). The gray shading around the line represents a confidence interval of 0.95.

Molecular characteristics landscape of GC with PET score

To investigate the molecular characteristics in gastric cancer with PETscore, we utilized the Cancer Genome Atlas (TCGA). PETscore was compared with glucose metabolic profiles. The PETscore was positively correlated with GLUT and glycolysis signatures ($r = 0.26$, P -value < 0.0001 for GLUT; **Figure 14A**, $r = 0.26$, P -value < 0.0001 for glycolysis; **Figure 14B**). In addition, we confirmed that patients with stomach adenocarcinoma or tubular stomach adenocarcinoma had significantly higher PETscore than diffuse type gastric cancer (P -value = 0.0206 for stomach type, P -value = 0.0077 for tubular type; **Figure 15**). Interestingly, PETscore tended to be associated with microsatellite instability (MSI) status. The PETscore of GC with MSI-high (MSI-H) was significantly higher than those of MSI-low (MSI-L) and MSS tumors (**Figure 16A**). As MSI status affects tumor mutational burden (TMB), the correlation analysis between TMB and PETscore was performed. Accordingly, PETscore showed a significant positive correlation with TMB ($R = 0.29$, P -value = $2.1e-8$) (**Figure 16B**). The comprehensive illustration of the molecular characteristic landscape is depicted in **Figure 17**. Additionally, we investigated the genomic alteration of each group from gastric cancer divided by the median enrichment scores of PETscore. Four genes (*PLXNA3*, *EIF4G1*, *TRIO*, *PCNX*) were identified as frequently mutated genes in high PETscore group (**Figure 18**). An a further investigation, we performed survival

analysis using TCGA and Asian Cancer Research Group (ACRG) with PETscore for all subjects. There was no significant association with survival depending on MSI/PETscore subgroups in TCGA cohort (**Figure 19A, B**). However, overall survival with PETscore in ACRG cohort showed significant difference (P -value=0.007) (**Figure 19C**). Furthermore, epithelial-mesenchymal transition (EMT) with low PETscore subgroup in ACRG cohort showed poor survival (P -value=0.007) (**Figure 19D**). Association between Lauren types and PETscore showed a trend that samples with high PETscore is located within intestinal type (P -value = 0.0023) (**Figure 19E**). Overall survival of Lauren types with PETscore showed significant difference. Diffuse type with low PETscore group showed poor survival (P -value = 0.0016) (**Figure 19F**).

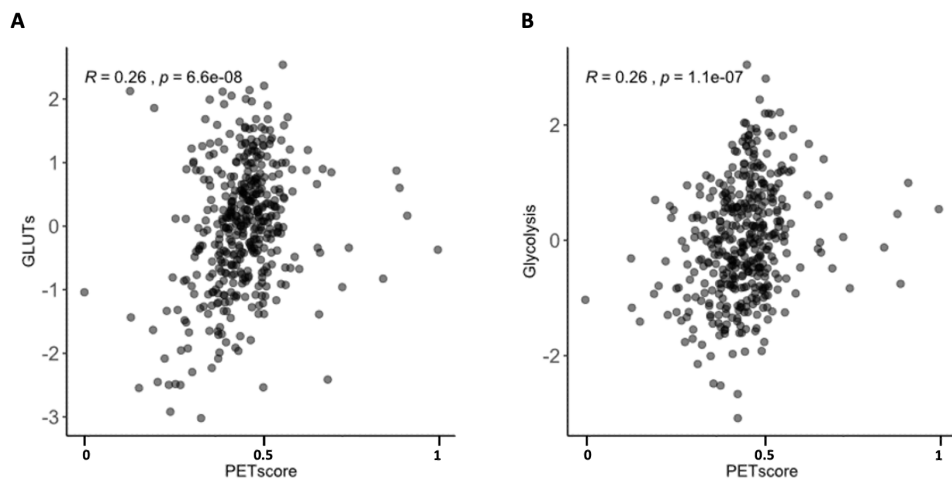


Figure 14. Molecular characteristic landscape of gastric cancer with PETscore. Scatter plot of PETscore versus GLUT and glycolysis signatures. (A, B) Both GLUT and glycolysis signatures are positively correlated with PETscore by Pearson's correlation ($r = 0.26$, P -value < 0.0001).

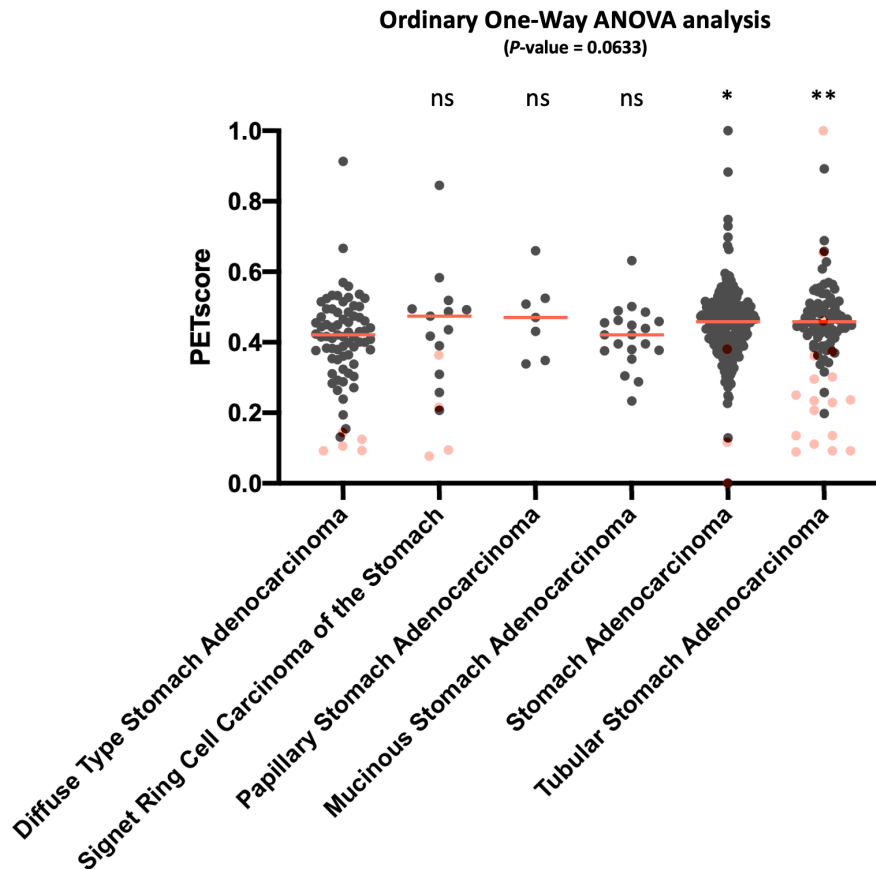


Figure 15. Association between PETscore and gastric cancer type. Tubular and stomach types show significant median value difference of PETscore compared with diffuse type (P -value = 0.0206 for stomach type, P -value = 0.0077 for tubular type). Red dots indicate PETscores of the thirty PET-scanned PDXs.

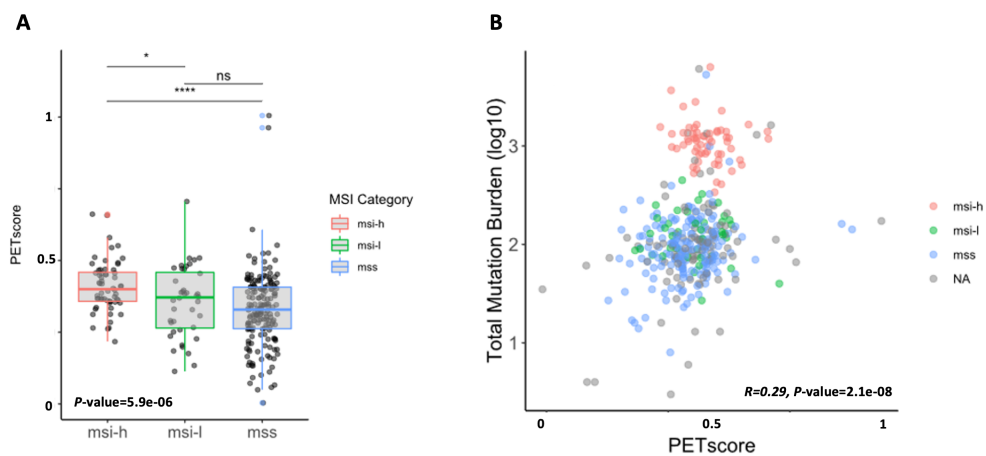


Figure 16. Association between PETscore and microsatellite instability. (A) The PETscore is significantly clustered between the MSI status. (B) The colored dots indicate MSI status of each sample, and it shows a trend that samples with high mutation burden are located within populations with high PETscore.

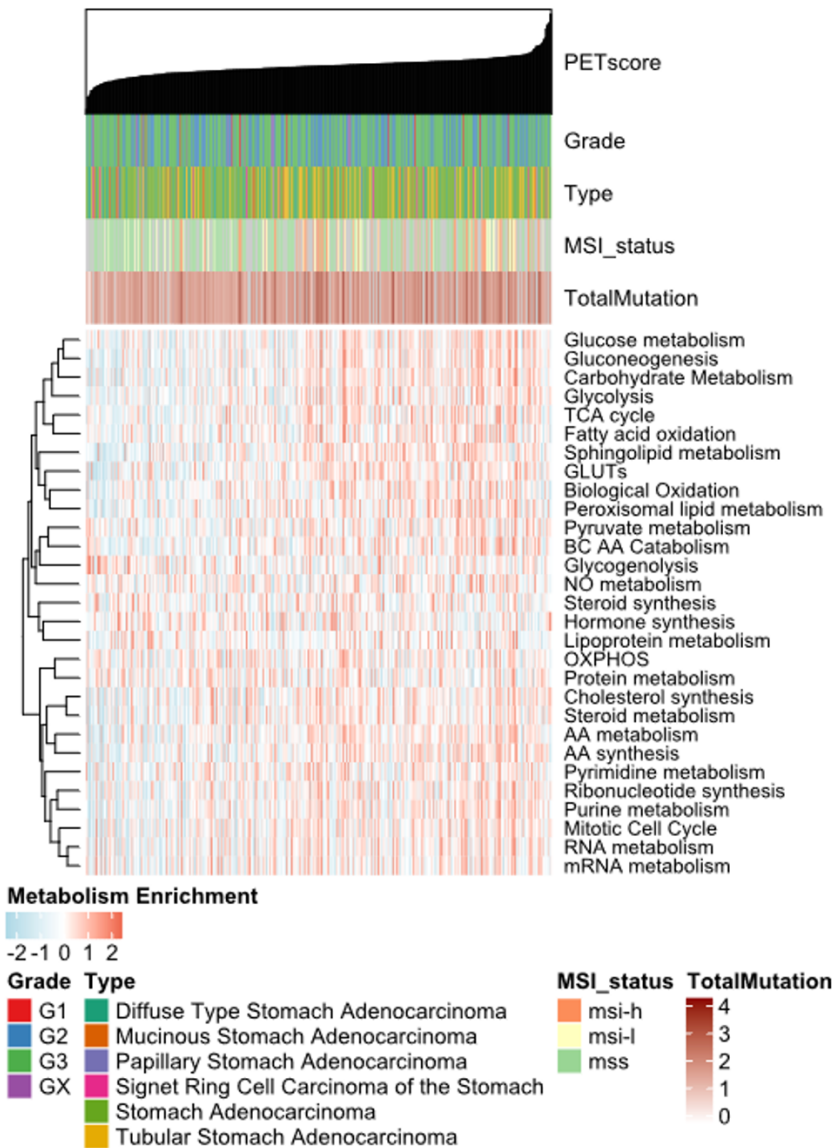


Figure 17. The comprehensive illustration showing the relationship between molecular characteristic landscape and PETscore. A heatmap depicting the metabolism enrichment scores of all samples. Grade, type by WHO classifications, MSI status, and total mutation are shown for each sample (above the heatmap).

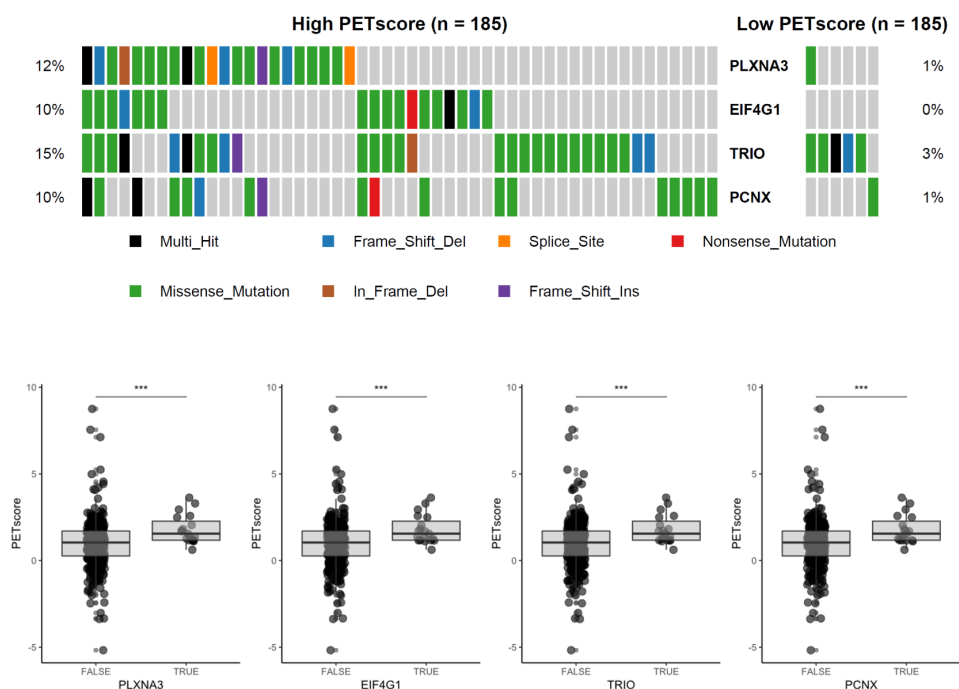
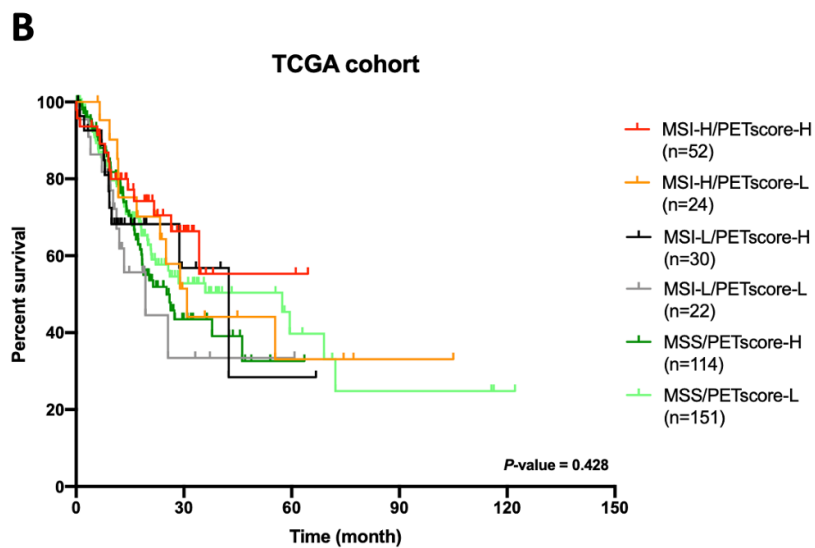
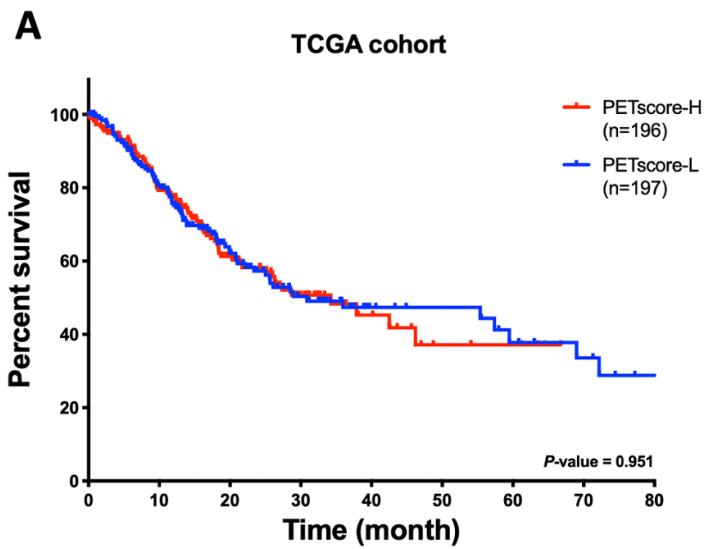
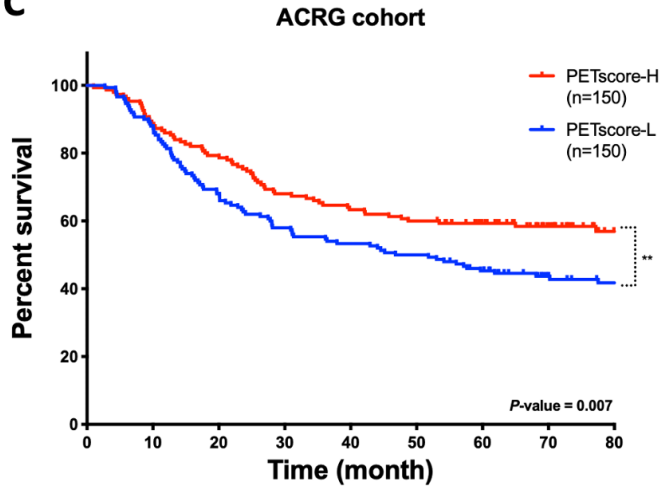
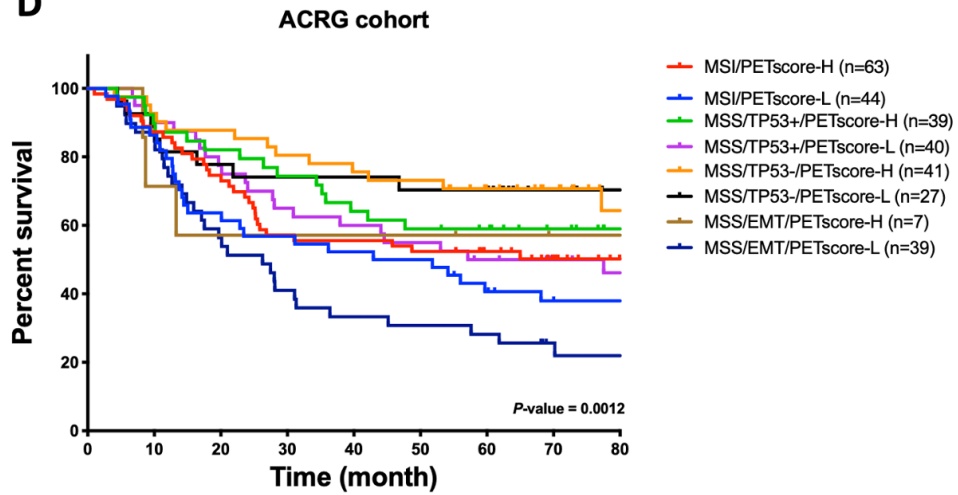


Figure 18. Genomic alterations associated with PETscore in gastric cancer. Each oncoplot (the upper panel) shows the genomic alteration of each group from gastric cancer divided by the median enrichment score of PETscore. Four genes (*PLXNA3*, *EIF4G1*, *TRIO* and *PCNX*) are frequently mutated genes between two groups. The lower panel shows gastric cancer sample distribution in each gene.



C**D**

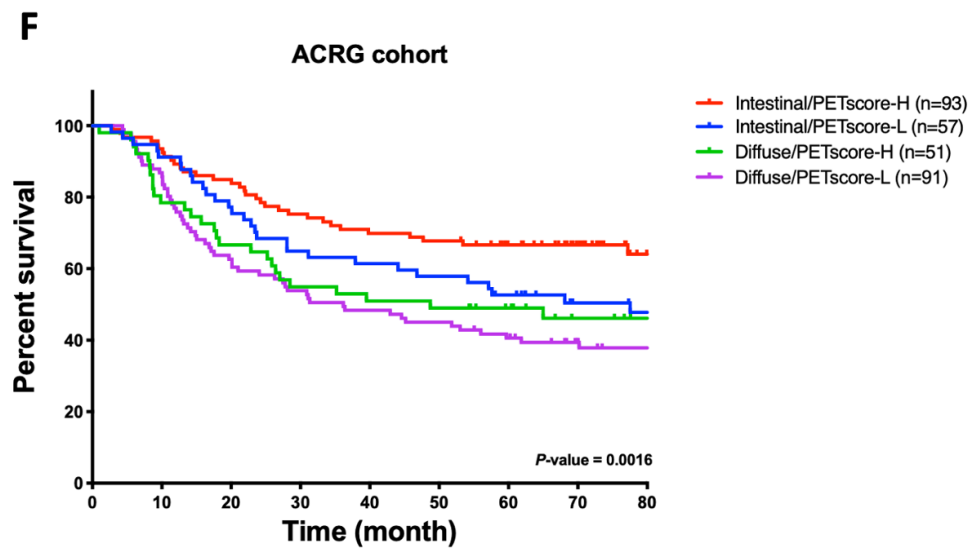
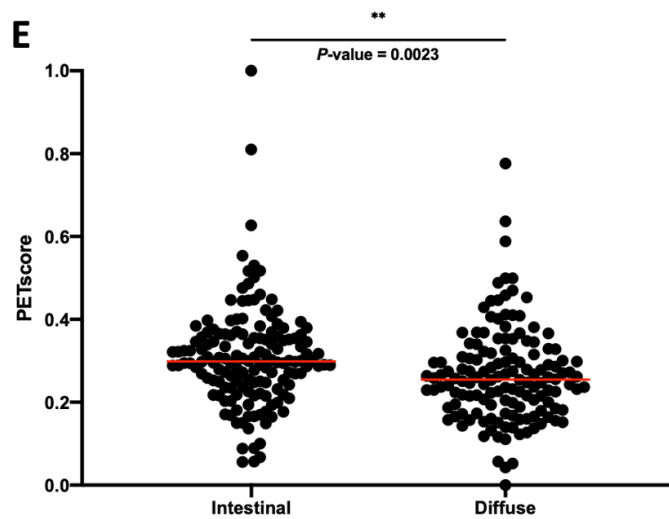
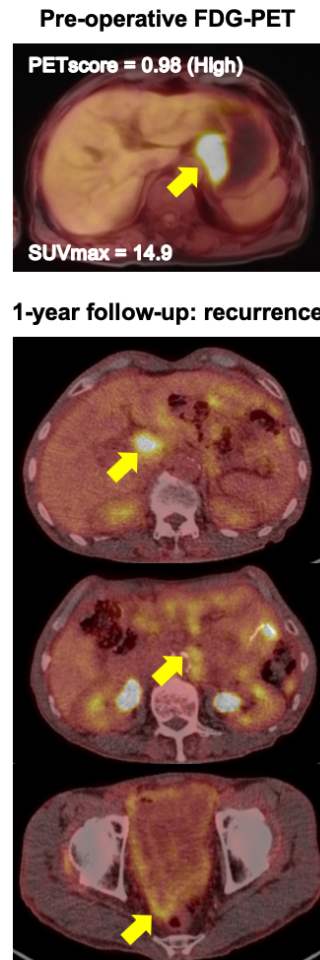


Figure 19. Survival analysis with PETscore using TCGA and ACRG data. (A) Association of PETscore with overall survival in TCGA cohort (P -value=0.951). (B) Association of MSI subgroups with overall survival in TCGA cohort (P -value=0.428). (C) Association of PETscore with overall survival in ACRG cohort. High PETscore group shows significantly better survival than low PETscore groups (P -value=0.007). (D) Association of molecular subgroups with overall survival in ACRG cohort. EMT type with low PETscore group shows significantly worse survival than the 7 other groups (P -value = 0.0012). (E) Association between PETscore and Lauren classification in ACRG cohort. The result shows a trend that samples with high PETscore is located within intestinal type (P -value = 0.0023). (F) Association of Lauren subgroups with overall survival in ACRG cohort. Intestinal group with high PETscore indicates significantly better survival than the 3 other groups (P -value = 0.0016).

A



B



C

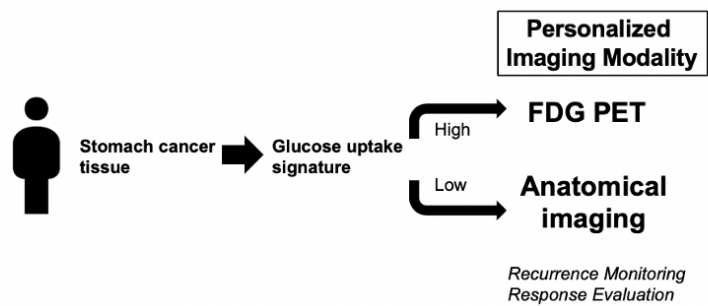
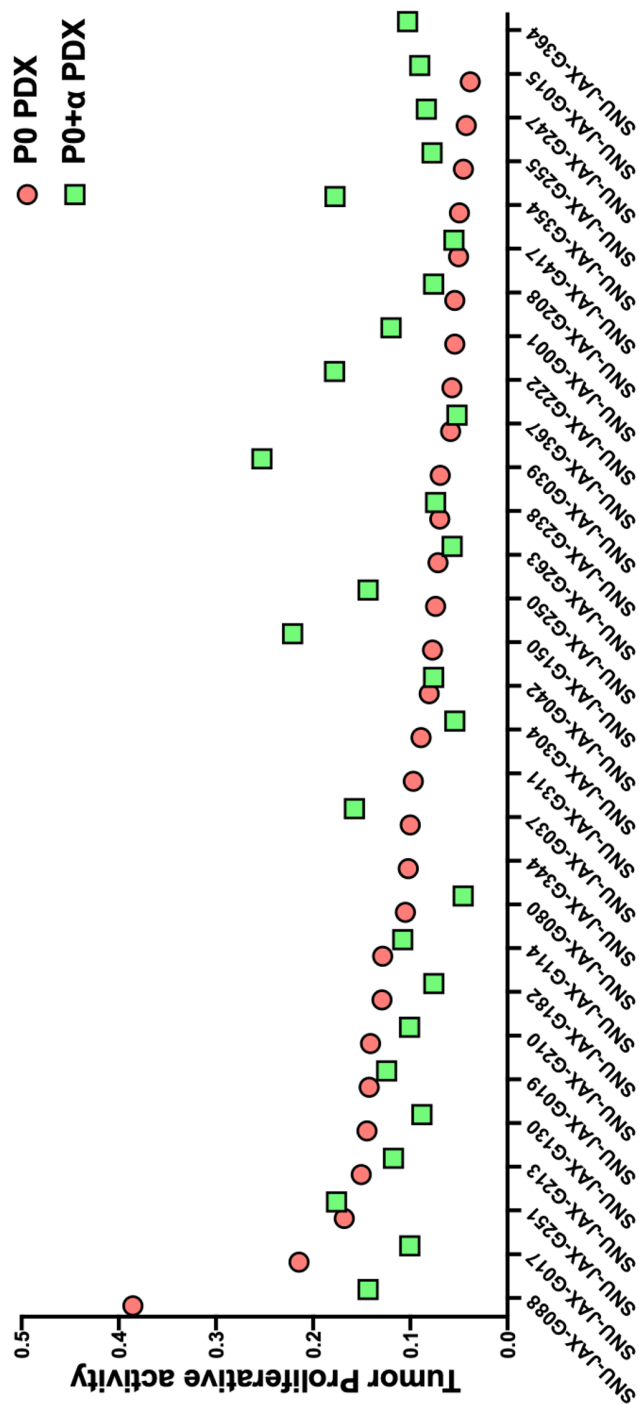
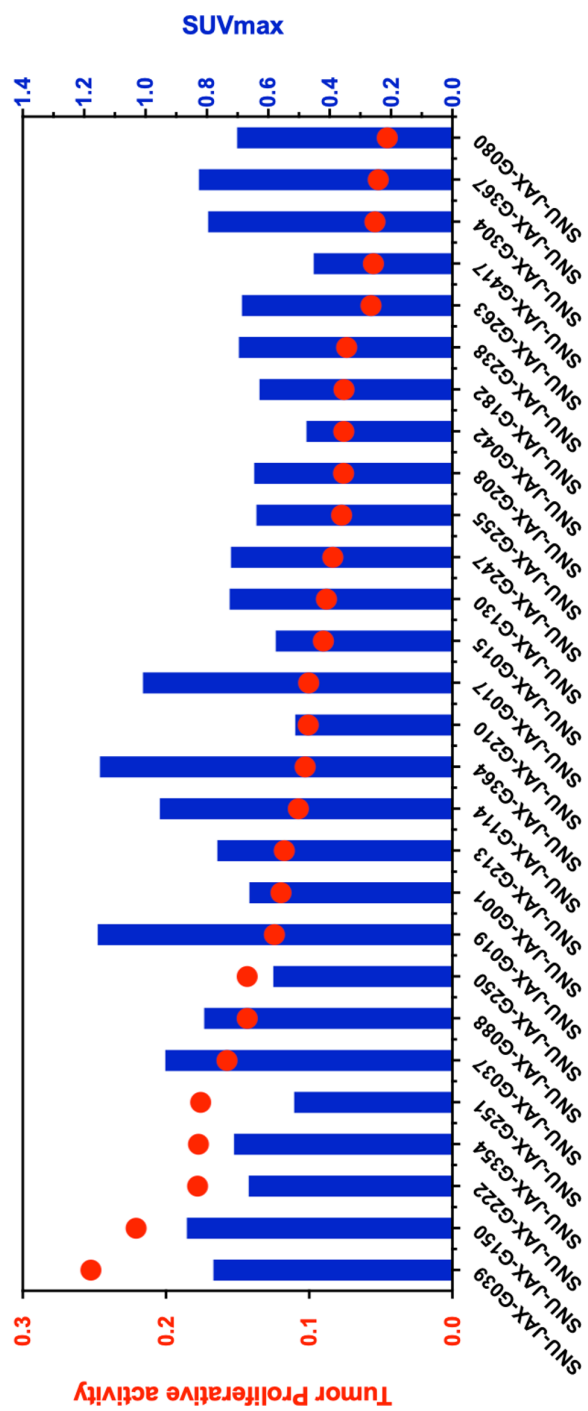


Figure 20. Examples in clinical application with the PETscore. (A) PET/MRI images of gastric cancer patient with low PETscore. 1-year follow-up shows recurrence with peritoneal seeding nodules (False-negative SUVmax). FDG-PET may be worse for this patient to monitor tumors. (B) PET/MRI images of gastric cancer patient with high PETscore. 1-year follow-up shows recurrence with high FDG-avid lymph nodes (SUVmax = 9.5) and peritoneal wall (SUVmax = 4). FDG-PET may be better for this patient to monitor tumors. (C) Schematic figure for personalized gastric cancer imaging

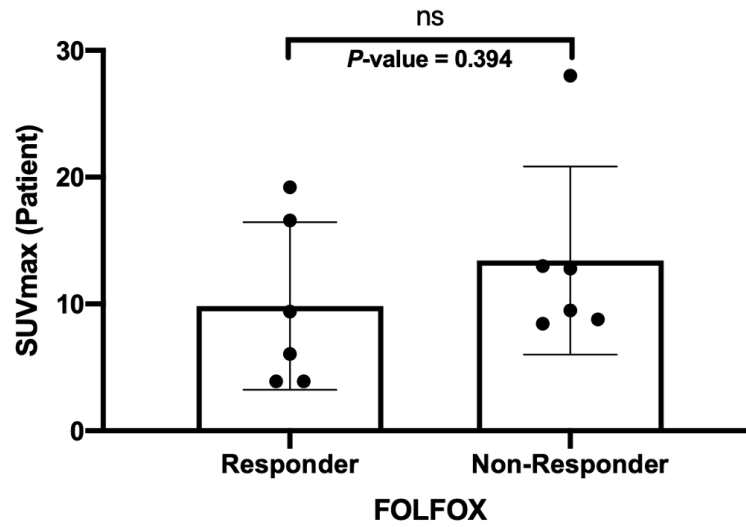
A



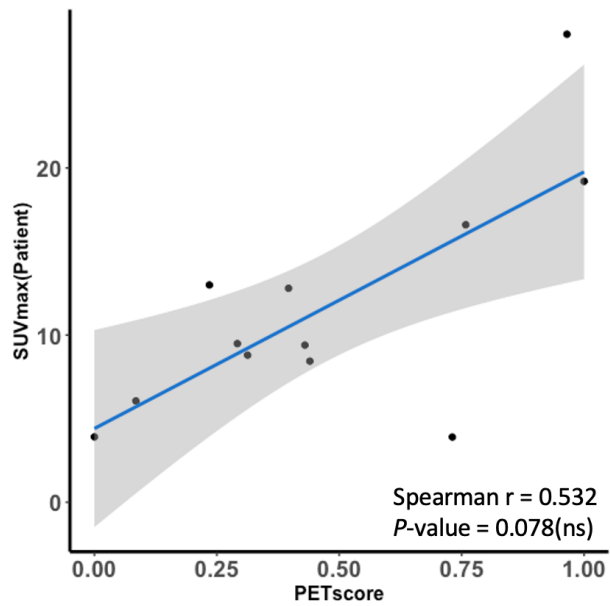
B



C



D



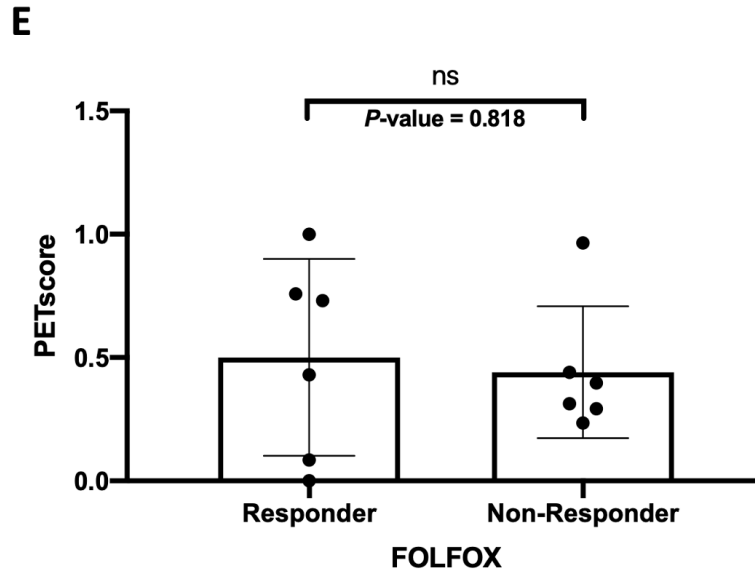


Figure 21. Investigation of FOLFOX sensitivity-related SUVmax and PETscore in human. (A) Tumor proliferative activity in P0 and P0+ α PDX tumors where integer $\alpha \geq 1$. Tumor proliferative activity is defined as “1/doubling time (day)”. (B) Comparison between SUVmax and tumor proliferative activity (Spearman $r = 0.238$, P -value = 0.224). (C) FDG avidity in response and non-response groups to FOLFOX. (D) Correlation analysis between PETscore and SUVmax (Spearman $r = 0.532$, P -value = 0.078). (E) FDG avidity by PETscore in response and non-response groups to FOLFOX.

Table 6. Correlation analysis between SUVmax/PETscore and EMT-related *HIF1A* downstream

Gene name	HIF1A	CDH1	DSP	TJP1	VIM	CDH2	SNAI1	SNAI2	TWIST1	ZEB1	ZEB2	MMP2	MMP3	MMP9
Spearman r (SUVmax)	0.3802	0.1586	-0.1181	0.2899	-0.1132	0.1995	0.04917	-0.1122	0.02182	0.24	0.1693	-0.2037	0.143	-0.3463
P-value	0.0382	0.4025	0.5341	0.1202	0.5513	0.2906	0.7964	0.5551	0.9089	0.2014	0.3711	0.2803	0.4509	0.0609
P-value summary	*	ns	ns	ns	ns	ns	ns	ns	ns	ns	ns	ns	ns	ns
Spearman r (PETscore)	0.4087	0.2739	-0.119	0.08476	0.09232	0.2253	0.1168	0.06649	0.3152	0.2258	0.3059	-0.03436	0.1335	0.05373
P-value	0.0249	0.1431	0.531	0.6561	0.6275	0.2313	0.5388	0.727	0.0898	0.2302	0.1002	0.857	0.4818	0.7779
P-value summary	*	ns	ns	ns	ns	ns	ns	ns	ns	ns	ns	ns	ns	ns

DISCUSSION

In this study, we used human gastric cancer patient-derived xenograft (PDX) models with small animal [^{18}F]FDG-PET images to develop a FDG avidity prediction model. We utilized systems biology approach, applying WGCNA to identify transcriptomic correlates of the maximum standardized uptake value (SUVmax) in gastric cancer. A significant gene network module correlated with [^{18}F]FDG avidity in PDX mouse models and a prediction model (PETscore) developed using the module predicted actual SUVmax in human. Furthermore, PETscore was associated with microsatellite instability (MSI) status, epithelial mesenchymal transition (EMT) and patients' survival.

Preclinical PET imaging PDX murine models

To our knowledge this is the first study to evaluate such model on an [^{18}F]FDG-PET/MRI with different imaging protocols and PDX implantation methods. Our results demonstrate a stable data quality using a fixed scanning protocol using 150 μCi . In heterotopic implantation, we did not identify distinguishable SUVmax difference in different tumor sizes with the same PDX tissues (**Figure 2B**). Although several studies have reported a positive correlation between SUVmax and tumor size (16–18), the correlation in gastric cancer specifically is controversial (19–21). Moreover, PET signal of big size tumors can

overlap with signals from other organs. Therefore, an appropriate tumor size to acquire the best image quality in *in-vivo* studies is required. In orthotopic implantation, even in immune-compromised mice, a confounding inflammation signal has to be considered for a period of 1-2 months, however, sufficient tumor growth in this setting usually exceeds this period.

In other solid cancer types, the [^{18}F]FDG-PET, mostly in combination with computer tomography in a preclinical research setting is established as a tool to investigate drug response or biological behavior (22, 23). Valtorta et al. introduced a PDX model of non-small cell lung cancer (NSCLC) for [^{18}F]FDG-PET/CT and demonstrated its usefulness of early therapy response evaluation in nine subcutaneous PDX tissues (24). The authors conclude that the imaging reflects the cancer glucose metabolism which correlates with tumor aggressiveness and growth in this study. Halderson et al. introduced an orthotopic endometrial cancer cell line model and outlined the usefulness of both [^{18}F]FDG and [^{18}F]FLT-PET/MRI for tumor growth monitoring and detection of metastasis (25). These abilities are important especially in orthotopic models, where often an external control of tumor growth is impossible.

Our study demonstrates [^{18}F]FDG-PET signals in both orthotopic and heterotopic PDX models. The images suggest that tumor monitoring in orthotopic gastric cancer models might benefit from MRI addition, thus several difficulties in orthotopic tumor modeling have to be

discussed. MRI has been used in several studies for monitoring the tumor growth and metastasis in orthotopic models (26, 27). However, long-term follow-up with MRI for monitoring tumor development, growth, and metastasis in preclinical studies, especially with a large number of mice, is expensive and time-consuming (28). A larger drop out of cases in orthotopic models has to be expected traditionally, therefore the benefits of a more natural tumor environment can be achieved. In terms of inflammatory signal overlapping, our results suggest that the SUVmax can be increased even after a longer period (Day 57) without tumor implantation (**Figure 5**), and was found in comparable levels as “healthy controls”. It is strongly recommended to always correlate the FDG signal in orthotopic models with the histology in order not to deal with problems of false positivity. The results of the GLUT1 and HK2 IHC staining therefore suggest, that a higher marker expression appears in orthotopic model’s tumor tissue, which goes along with a higher glucose uptake detected by PET, possible reflecting the alternated tumor environment in orthotopic implantation. The IHC staining results give a rational explanation for higher FDG avidity in orthotopic tumor modeling beyond an inflammatory confounder as tumor tissue was measured for relevant protein levels. Thus, the technical difficulty of tumor implantation and a more resource consuming monitoring has to be considered when applying an orthotopic model in a high-throughput study.

Using a PET/MRI may consume more human and financial

resources than a single PET scanner. However, anatomical conditions might aggravate the signal detection in orthotopic models as the left kidney signal is found close and sometimes overlapping to the stomach site. Again, forth is reason, the MRI provides the best possible resolution to allocate uptake signal to an anatomical structure.

The major limitation of our study is the small sample size of the PDX case. Further studies utilizing larger sample sizes of different PDXs are necessary in order to understand and describe glucose uptake relation between gastric cancer patients and corresponding PDXs.

PETscore: a FDG avidity prediction model

The clinical utility of FDG-PET in GC is influenced by factors including tumor size, histological subtype, tumor location and physiological FDG uptake by normal gastric wall (40). GC has varying sensitivities of FDG-PET due to tumor biological heterogeneity. As prediction of FDG uptake will be critical role for rational gastric cancer patient selection, we sought to develop a prediction model for [^{18}F]FDG avidity in GC.

PDX models have shown advantages as a useful preclinical resource in drug screening, bio-marker development and co-clinical trial. Despite of disadvantage with low enraft rates and high costs, one of main advantages is that PDXs allow the propagation and expansion of patient tumors without significant genetic

change of tumor cells over multiple generations (41). Moreover, PDX models are beneficial to studies for certain drugs response and imaging because multiple tests are available expending PDXs generated from one parental tumor. Our result of FDG avidity correlation between PDXs and patients suggested that PDXs, as surrogates, can be utilized for PET activity studies reflecting glucose metabolism in patient tumors (Spearman $r = 0.54$, P -value = 0.04, **Figure 10C**). Therefore, PDXs with genomic data and PET imaging results are considered as useful materials to investigate the heterogeneous FDG avidity in GC mimicking patient tumors.

We have found a gene signature with 4 positively correlated genes (*PLS1*, *PYY*, *SLC6A5*, *HBQ1*) and one negatively correlated gene (*NAT16*) which is associated with SUVmax by co-expression network analysis. *PLS1* gene encodes pastin 1 protein which is a member of the platin (also known as fimbrin) family and the family is one of actin-binding proteins, and it is evolutionarily conserved (42). Platins are expressed in various cancers including choroids plexus tumors (43), urinary bladder cancer (44), ovarian cancer (45), and colorectal cancer (46). PeptideYY (*PYY*) is a gut hormone and its expression increases sequentially along the length of the intestines (47, 48). *PYY* with hormonal regulation of upper gastrointestinal function causes decreased gastric acid secretion, delays gastric emptying and slows intestinal transit time (47, 49). *PYY* has been identified in several carcinoid tumors including rectal carcinoids (50), gastric,

small bowel and cecal endocrine tumors (51, 52). Moreover, a decreased expression of *PYY* may be relevant to the development and progression of colon adenocarcinoma (53, 54). Solute Carrier Family 6 Member 5 (*SLC6A5*), Hemoglobin Subunit Theta 1 (*HBQ1*), and N-Acetyltransferase 16 (*NAT16*), which are protein coding genes, have not been well defined in cancer biology, particularly in GC.

The prediction model with the signature (PETscore) was validated inhuman using RNA-seq and qRT-PCR data. RNA-seq and qRT-PCR provide a value can be calculated for the concentration of a target region in a given sample (55). RNA-seq has been developed as a powerful method for investigating the intracellular transcriptome level based on next generation sequencing (NGS) and widely used in translational research (56). Although high throughput sequencing (HTS) methods for analyzing RNA have been improving, qRT-PCR is still a routine and cost-effective method for precise and accurate mRNA analysis (57, 58). qRT-PCR has, however, limitation with utilizing amplicons smaller than 300bp, usually toward the 3' end of the coding region, avoiding the 3' untranslated region(3'UTR) (59). Despite of the gap between two platforms, our PETscore provides applicability for prediction of FDG uptake (**Figure 13B, C**). Our suggested model could be used in the clinical setting to perform individualized approach for choosing imaging modality for the assessment of GC. As a glucose uptake pattern non-invasively assessed by [¹⁸F]FDG-PET is a unique

biological feature, it is maintained in recurred tumor. Thus, if we predict [^{18}F]FDG avidity before staging or recurrence monitoring, [^{18}F]FDG-PET may be selectively used for a tumor which expects to show high [^{18}F]FDG-avid tumor. A tumor which showed the low PETscore was also low FDG avidity in are curred tumor at 1-year follow-up. On the other hand, another tumor with high PETscore showed hypermetabolim in recurred retroperitoneal LNs and peritoneal seeding lesions. The example cases are shown in **Figure 20A, B**. Furthermore, as the gene signature can be assessed by biopsy tissues, the PETscore can be used for an individualized approach for imaging modality (**Figure 20C**). These findings provide the opportunity to include a rational selection process for gastric cancer [^{18}F]FDG-PET clinical evaluation. Further well-designed clinical validation of this suggested individualized imaging for GC is warranted.

FOLFOX is one of the gastric cancer chemotherapeutic regimens being widely, which is the combination of folinic acid (FOL), 5-fluorouracil (F) and oxaliplatin (OX). 5-fluorouracil (5-FU) as a main component in FOLFOX which is a type of fluoropyrimidine that incorporates into DNA to inhibit thymidylate synthase (TS). Oxaliplatin (trans-/-diaminocyclohexane oxalatoplatinum; L-OHP) is a platinum-based antineoplastic agent that inhibits DNA replication and transcription by forming cross linkages within double strands of DNA. Folinic acid stabilizes the 5-FU-TS complex with less cytotoxicity and reduced side effects of 5-FU with lower dosage which is required to

complete the cycles of treatment. We primarily investigated the tumor doubling time of PDXs because uncontrolled proliferation is one of cancer hallmarks. There was no difference on doubling time between P0 and passaged ($P0+\alpha$, where integer $\alpha \geq 1$) PDX tumors (compared by Mann-Whitney U test, P -value = 0.202, **Figure 21A**). Unlike what we expected, the proliferative activity with doubling time was not correlated the FDG avidity in PDX tumors (Spearman $r = 0.238$, P -value = 0.224, **Figure 21B**). Based on the results of FOLFOX groups in GC PDXs, we investigated the FDG avidity in twelve PET-scanned patients. We found the slight tendency with high SUVmax in FOLFOX non-responder group. However, there was no significant difference for SUVmax or PETscore between the responder and non-responder groups (**Figure 21 C, D**).

GC with microsatellite instability high (MSI-H) was proposed as a distinct subgroup of GCs characterized by two large scale molecular studies, The Cancer Genome Atlas (TCGA) and the Asian Cancer Research Group (ACRG) classification (60, 61). Choi et al. reported that STAD (Stomach Adenocarcinoma) and COAD (Colon adenocarcinoma) showed a large number of the metabolism-related genes than other cancer types investigating the relationship between metabolic profiles and MSI status (36). Our results also showed that MSI-H with high PETscore had hypermutation burden (**Figure 16B, 17**). MSI-H GCs are more likely to have favorable survival than low level MSI (MSI-L) or microsatellite

stable (MSS) tumors and associated with both high Tumor-infiltrating lymphocytes (TILs) and programmed death-ligand 1 (PD-L1) (62-65). Moreover, accurate and reliable evaluation of MSI status considered as a biomarker for therapeutics with immune-checkpoint inhibitors is important (66, 67).

The epithelial-mesenchymal transition (EMT) is critical role in embryonic development, wound healing and fibrotic disease (68, 69). Tumors poorly infiltrated by T-cells, commonly referred to as “cold” tumors, are associated with resistance of response to immune checkpoint blockade (70). Cold tumors has been reported the linkage with EMT which is well-known as one of cancer aggressiveness hallmarks with poor survival. Various factors including hypoxia could induce and aggravate GC via EMT, which is significantly correlated with prognosis. We found that PETscore-Low (PETscore-L) and MSS/EMT/PETscore-L had a poor prognosis in the ACRG cohort (**Figure 19C, D**).

Takebayashi et al. have reported that SUVmax in gastric cancer is rather related to hypoxic status, not the glycolytic gene expressions (71). Indeed, our investigation of hypoxia inducible factor 1 alpha (*HIF1A*) and EMT-related its downstream comparing SUVmax showed that *HIF1A* had weak positive correlation (Spearman $r = 0.38$, P -value = 0.04, **Table 6**). In this regards, our results suggest that PETscore, as a bio-imaging marker identifying “cold tumors”, could be used to estimate prognosis in GC.

Limitations

The present study has certain limitations. First, although we identified a gene signature using small animal PET images and RNA-seq data of human GC PDXs and genomic alterations based on our PETscore, functional analysis with the consequent genes are necessary to further understand the functions of these genes in FDG uptake regulation of gastric cancer. Second, an additional analysis with histopathologic data will make our results more solid and reliable. We only used PET image results and mRNA transcriptome data of PDX tumor for developing the prediction model. Even though our prediction model (PETscore) showed clinical characteristics similar to FDG uptake reported in previous literature, comprehensive multi modal analysis including transcriptome, imaging, and histopathologic data can improve our results. Finally, we developed PETscore based on RNA-seq data, which predicts tumor SUVmax; however, PETscore should be cautiously used according to independent external gene expression data. As we applied PETscore for qRT-PCR data, the data was needed to be preprocessed due to the scale difference on gene expression levels.

Conclusion

We have introduced a specific [^{18}F]FDG-PET protocol for orthotopic and heterotopic gastric cancer PDX in PART I. Heterotopic model has higher success rate with less mortality. We confirmed correlation with common

[¹⁸F]FDG-PET related tissue markers and distinct tumor signal. PDX mouse model can be useful to access PET activity in gastric cancer.

In PART II, we identified a five-gene signature for FDG uptake prediction in gastric cancer using PDXs, which was validated by RNA-seq and qRT-PCR in human. We found PETscore associations for glycolytic signature and EMT-related prognosis in public omics databases.

Thus, as a strength of this study is can be mentioned that this is the first study to establish a clinically relevant genetic signature of gastric cancer likely to show high FDG uptake. Our PETscore may provide additional information for gastric cancer patient selection for personalized PET imaging.

REFERENCES

1. Bae S-W, Berlth F, Jeong K-Y, Suh Y-S, Kong S-H, Lee H-J, et al. Establishment of a [18F]-FDG-PET/MRI Imaging Protocol for Gastric Cancer PDX as a Preclinical Research Tool. *J Gastric Cancer*. 2020;20:60-71.
2. Gullo I, Carneiro F, Oliveira C, Almeida GM. Heterogeneity in Gastric Cancer: From Pure Morphology to Molecular Classifications. *Pathobiology*. 2018;85:50-63.
3. Vergadis C, Schizas D. Is Accurate N - Staging for Gastric Cancer Possible? *Front Surg*. 2018;5:41.
4. Rigo P, Paulus P, Kaschten BJ, Hustinx R, Bury T, Jerusalem G, et al. Oncological applications of positron emission tomography with fluorine-18 fluorodeoxyglucose. *Eur J Nucl Med*. 1996;23:1641-74.
5. Bomanji JB, Costa DC, Ell PJ. Clinical role of positron emission tomography in oncology. *Lancet Oncol*. 2001;2:157-64.
6. Yuan LW, Yamashita H, Seto Y. Glucose metabolism in gastric cancer: The cutting-edge. *World J Gastroenterol*. 2016;22:2046-59.
7. Liberti MV, Locasale JW. The Warburg Effect: How Does it Benefit Cancer Cells? *Trends Biochem Sci*. 2016;41:211-8.
8. Kim SK, Kang KW, Lee JS, Kim HK, Chang HJ, Choi JY, et al. Assessment of lymph node metastases using

- 18F-FDG PET in patients with advanced gastric cancer. Eur J Nucl Med Mol Imaging. 2006;33:148-55.
9. Yeung HW, Macapinlac H, Karpeh M, Finn RD, Larson SM. Accuracy of FDG-PET in Gastric Cancer. Preliminary Experience. Clin Positron Imaging. 1998;1:213-21.
 10. Stahl A, Ott K, Weber WA, Becker K, Link T, Siewert JR, et al. FDG PET imaging of locally advanced gastric carcinomas: correlation with endoscopic and histopathological findings. Eur J Nucl Med Mol Imaging. 2003;30:288-95.
 11. Mochiki E, Kuwano H, Katoh H, Asao T, Oriuchi N, Endo K. Evaluation of 18F-2-deoxy-2-fluoro-D-glucose positron emission tomography for gastric cancer. World J Surg. 2004;28:247-53.
 12. Chen J, Cheong JH, Yun MJ, Kim J, Lim JS, Hyung WJ, et al. Improvement in preoperative staging of gastric adenocarcinoma with positron emission tomography. Cancer. 2005;103:2383-90.
 13. Yun M, Lim JS, Noh SH, Hyung WJ, Cheong JH, Bong JK, et al. Lymph node staging of gastric cancer using (18)F-FDG PET: a comparison study with CT. J Nucl Med. 2005;46:1582-8.
 14. De Potter T, Flamen P, Van Cutsem E, Penninckx F, Filez L, Bormans G, et al. Whole-body PET with FDG for the diagnosis of recurrent gastric cancer. Eur J Nucl Med Mol Imaging. 2002;29:525-9.
 15. Bhimani J, Ball K, Stebbing J. Patient-derived

- xenograft models—the future of personalised cancer treatment. *Br J Cancer*. 2020;122:601–2.
16. Yoshida GJ. Applications of patient-derived tumor xenograft models and tumor organoids. *J Hematol Oncol*. 2020;13:4.
 17. Avril N, Menzel M, Dose J, Schelling M, Weber W, Janicke F, et al. Glucose metabolism of breast cancer assessed by ¹⁸F-FDG PET: histologic and immunohistochemical tissue analysis. *J Nucl Med*. 2001;42:9–16.
 18. Takebayashi R, Izuishi K, Yamamoto Y, Kameyama R, Mori H, Masaki T, et al. [¹⁸F]Fluorodeoxyglucose accumulation as a biological marker of hypoxic status but not glucose transport ability in gastric cancer. *J Exp Clin Cancer Res*. 2013;32:34.
 19. Kim JS, Park SY. (¹⁸F)-FDG PET/CT of advanced gastric carcinoma and association of HER2 expression with standardized uptake value. *Asia Ocean J Nucl Med Biol*. 2014;2:12–8.
 20. Ahn KS, Kang KJ, Kim YH, Kim TS, Song BI, Kim HW, et al. Genetic features associated with (¹⁸F)-FDG uptake in intrahepatic cholangiocarcinoma. *Ann Surg Treat Res*. 2019;96:153–61.
 21. Euhus DM, Hudd C, LaRegina MC, Johnson FE. Tumor measurement in the nude mouse. *J Surg Oncol*. 1986;31:229–34.
 22. Tomayko MM, Reynolds CP. Determination of subcutaneous tumor size in athymic (nude) mice. *Cancer Chemother Pharmacol*. 1989;24:148–54.

23. Lai Y, Wei X, Lin S, Qin L, Cheng L, Li P. Current status and perspectives of patient-derived xenograft models in cancer research. *J Hematol Oncol.* 2017;10:106.
24. Choi YY, Lee JE, Kim H, Sim MH, Kim KK, Lee G, et al. Establishment and characterisation of patient-derived xenografts as preclinical models for gastric cancer. *Sci Rep.* 2016;6:22172.
25. Sulaiman A, Wang L. Bridging the divide: preclinical research discrepancies between triple-negative breast cancer cell lines and patient tumors. *Oncotarget.* 2017;8:113269-81.
26. Fueger BJ, Czernin J, Hildebrandt I, Tran C, Halpern BS, Stout D, et al. Impact of animal handling on the results of 18F-FDG PET studies in mice. *J Nucl Med.* 2006;47:999-1006.
27. Ko GB, Yoon HS, Kim KY, Lee MS, Yang BY, Jeong JM, et al. Simultaneous Multiparametric PET/MRI with Silicon Photomultiplier PET and Ultra-High-Field MRI for Small-Animal Imaging. *J Nucl Med.* 2016;57:1309-15.
28. Jacobson O, Chen X. PET designated fluoride-18 production and chemistry. *Curr Top Med Chem.* 2010;10:1048-59.
29. Goulding H, Pinder S, Cannon P, Pearson D, Nicholson R, Snead D, et al. A new immunohistochemical antibody for the assessment of estrogen receptor status on routine formalin-fixed tissue samples. *Hum Pathol.* 1995;26:291-4.

30. Cho SY, Sung CO, Chae J, Lee J, Na D, Kang W, et al. Alterations in the Rho pathway contribute to Epstein-Barr virus-induced lymphomagenesis in immunosuppressed environments. *Blood*. 2018;131:1931-41.
31. Langfelder P, Horvath S. WGCNA: an R package for weighted correlation network analysis. *BMC Bioinformatics*. 2008;9:559.
32. Friedman J, Hastie T, Tibshirani R. Regularization Paths for Generalized Linear Models via Coordinate Descent. *J Stat Softw*. 2010;33:1-22.
33. Livak KJ, Schmittgen TD. Analysis of relative gene expression data using real-time quantitative PCR and the $2^{-\Delta\Delta C(T)}$ Method. *Methods*. 2001;25:402-8.
34. Colaprico A, Silva TC, Olsen C, Garofano L, Cava C, Garolini D, et al. TCGAAbiolinks: an R/Bioconductor package for integrative analysis of TCGA data. *Nucleic Acids Res*. 2016;44:e71.
35. Mayakonda A, Lin DC, Assenov Y, Plass C, Koeffler HP. Maftools: efficient and comprehensive analysis of somatic variants in cancer. *Genome Res*. 2018;28:1747-56.
36. Choi H, Na KJ. Pan-cancer analysis of tumor metabolic landscape associated with genomic alterations. *Mol Cancer*. 2018;17:150.
37. Liberzon A, Subramanian A, Pinchback R, Thorvaldsdottir H, Tamayo P, Mesirov JP. Molecular signatures database (MSigDB) 3.0. *Bioinformatics*.

- 2011;27:1739-40.
38. Wickham H. (2009). *Ggplot2 : elegant graphics for data analysis* (viii, pp212). New York: Springer.
 39. Ritchie ME, Phipson B, Wu D, Hu Y, Law CW, Shi W, et al. *limma* powers differential expression analyses for RNA-sequencing and microarray studies. *Nucleic Acids Res.* 2015;43:e47.
 40. Wu CX, Zhu ZH. Diagnosis and evaluation of gastric cancer by positron emission tomography. *World J Gastroenterol.* 2014;20:4574-85.
 41. Reyat F, Guyader C, Decraene C, Lucchesi C, Auger N, Assayag F, et al. Molecular profiling of patient-derived breast cancer xenografts. *Breast Cancer Res.* 2012;14:R11.
 42. Shinomiya H. *Plastin* family of actin-bundling proteins: its functions in leukocytes, neurons, intestines, and cancer. *Int J Cell Biol.* 2012;2012:213492.
 43. Hasselblatt M, Bohm C, Tatenhorst L, Dinh V, Newrzella D, Keyvani K, et al. Identification of novel diagnostic markers for choroid plexus tumors: a microarray-based approach. *Am J Surg Pathol.* 2006;30:66-74.
 44. Harris LD, De La Cerda J, Tuziak T, Rosen D, Xiao L, Shen Y, et al. Analysis of the expression of biomarkers in urinary bladder cancer using a tissue microarray. *Mol Carcinog.* 2008;47:678-85.
 45. Kang S, Shim HS, Lee JS, Kim DS, Kim HY, Hong SH, et al. Molecular proteomics imaging of tumor interfaces

- by mass spectrometry. J Proteome Res. 2010;9:1157-64.
46. Ang CS, Nice EC. Targeted in-gel MRM: a hypothesis driven approach for colorectal cancer biomarker discovery in human feces. J Proteome Res. 2010;9:4346-55.
47. Hazelwood RL. The pancreatic polypeptide (PP-fold) family: gastrointestinal, vascular, and feeding behavioral implications. Proc Soc Exp Biol Med. 1993;202:44-63.
48. Wilander E, El-Salhy M, Lundqvist M, Grimelius L, Terenius L, Lundberg JM, et al. Polypeptide YY (PYY) and pancreatic polypeptide (PP) in rectal carcinoids. An immunocytochemical study. Virchows Arch A Pathol Anat Histopathol. 1983;401:67-72.
49. Taylor IL. Role of peptide YY in the endocrine control of digestion. J Dairy Sci. 1993;76:2094-101.
50. Fiocca R, Rindi G, Capella C, Grimelius L, Polak JM, Schwartz TW, et al. Glucagon, glicentin, proglucagon, PYY, PP and proPP-icosapeptide immunoreactivities of rectal carcinoid tumors and related non-tumor cells. Regul Pept. 1987;17:9-29.
51. Hayashi H, Nakagawa M, Kitagawa S, Yamada T, Ishida K, Kurumaya H. Immunohistochemical analysis of gastrointestinal carcinoids. Gastroenterol Jpn. 1993;28:483-90.
52. Iwafuchi M, Watanabe H, Ishihara N, Shimoda T, Iwashita A, Ito S. Peptide YY immunoreactive cells in gastrointestinal carcinoids: immunohistochemical and

- ultrastructural studies of 60 tumors. *Hum Pathol.* 1986;17:291-6.
53. Calam J, Ghatei MA, Domin J, Adrian TE, Myszor M, Gupta S, et al. Regional differences in concentrations of regulatory peptides in human colon mucosal biopsy. *Dig Dis Sci.* 1989;34:1193-8.
54. Tari A, Miyachi Y, Sumii K, Kajiyama G, Miyoshi A. Peptide YY-like immunoreactivity in normal colon mucosa, muscle layer and adenocarcinoma. *Jpn J Med.* 1987;26:184-8.
55. Lowe R, Shirley N, Bleackley M, Dolan S, Shafee T. Transcriptomics technologies. *PLoS Comput Biol.* 2017;13:e1005457.
56. Wang Z, Gerstein M, Snyder M. RNA-Seq: a revolutionary tool for transcriptomics. *Nat Rev Genet.* 2009;10:57-63.
57. Costa C, Gimenez-Capitan A, Karachaliou N, Rosell R. Comprehensive molecular screening: from the RT-PCR to the RNA-seq. *Transl Lung Cancer Res.* 2013;2:87-91.
58. Dufva M. Comment on Wong and Medrano's "Real-time PCR for mRNA quantification" *BioTechniques* 39:75-85 (July 2005). *Biotechniques.* 2005;39:484; discussion 484-5.
59. Ramskold D, Wang ET, Burge CB, Sandberg R. An abundance of ubiquitously expressed genes revealed by tissue transcriptome sequence data. *PLoS Comput Biol.* 2009;5:e1000598.
60. Bass AJ, Thorsson V, Shmulevich I, Reynolds S.M,

- Miller M, Bernard B, et al. Comprehensive molecular characterization of gastric adenocarcinoma. *Nature*. 2014;513:202-9.
61. Cristescu R, Lee J, Nebozhyn M, Kim KM, Ting JC, Wong SS, et al. Molecular analysis of gastric cancer identifies subtypes associated with distinct clinical outcomes. *Nat Med*. 2015;21:449-56.
62. Falchetti M, Saieva C, Lupi R, Masala G, Rizzolo P, Zanna I, et al. Gastric cancer with high-level microsatellite instability: target gene mutations, clinicopathologic features, and long-term survival. *Hum Pathol*. 2008;39:925-32.
63. Fang WL, Chang SC, Lan YT, Huang KH, Chen JH, Lo SS, et al. Microsatellite instability is associated with a better prognosis for gastric cancer patients after curative surgery. *World J Surg*. 2012;36:2131-8.
64. Cho J, Chang YH, Heo YJ, Kim S, Kim NK, Park JO, et al. Four distinct immune microenvironment subtypes in gastric adenocarcinoma with special reference to microsatellite instability. *ESMO Open*. 2018;3:e000326.
65. Kim ST, Cristescu R, Bass AJ, Kim KM, Odegaard JI, Kim K, et al. Comprehensive molecular characterization of clinical responses to PD-1 inhibition in metastatic gastric cancer. *Nat Med*. 2018;24:1449-58.
66. Fuchs CS, Doi T, Jang RW, Muro K, Satoh T, Machado M, et al. Safety and Efficacy of Pembrolizumab Monotherapy in Patients With Previously Treated Advanced Gastric and Gastroesophageal Junction

- Cancer: Phase 2 Clinical KEYNOTE-059 Trial. *JAMA Oncol.* 2018;4:e180013.
67. Ratti M, Lampis A, Hahne JC, Passalacqua R, Valeri N. Microsatellite instability in gastric cancer: molecular bases, clinical perspectives, and new treatment approaches. *Cell Mol Life Sci.* 2018;75:4151-62.
68. Hay ED. The mesenchymal cell, its role in the embryo, and the remarkable signaling mechanisms that create it. *Dev Dyn.* 2005;233:706-720.
69. Lee JM, Dedhar S, Kalluri R, Thompson EW. The epithelial-mesenchymal transition: new insights in signaling, development, and disease. *J Cell Biol.* 2006;172:973-981.
70. Wang L, Saci A, Szabo PM, et al. EMT- and stroma-related gene expression and resistance to PD-1 blockade in urothelial cancer. *Nat Commun* 2018;9:3503.
71. Ryusuke Takebayashi , Kunihiro Izuishi, Yuka Yamamoto, Reiko Kameyama, Hirohito Mori, Tsutomu Masaki, et al. [18F]Fluorodeoxyglucose Accumulation as a Biological Marker of Hypoxic Status but Not Glucose Transport Ability in Gastric Cancer. *J Exp Clin Cancer Res.* 2013 May 29;32:34.

국문초록

배경: FDG-PET은 다양한 암의 병기, 약물반응 그리고 재발 평가에 널리 쓰이나, 위암의 경우 FDG의 섭취가 일정치 않아 그 역할이 제한적이다. 환자유래이종이식 모델(PDX)은 전임상 연구에서 유망한 *in-vivo* 모델이다. 본 연구는 환자맞춤 PET 계획 및 분자적 특성 조사를 위해 위암 PDX 마우스 모델을 이용한 FDG 섭취 예측 유전자 지표를 개발하는 것이다.

방법: 암컷 BALB/c 누드마우스에 위암 PDX 조직을 정위 및 피하에 이식했다. [^{18}F]FDG-PET 촬영 프로토콜을 다양한 종양 크기 및 FDG 선량, 촬영 간격 그리고 장기 특이적 FDG 섭취에 대해 평가했다. 동일 PDX를 이용한 정위 및 피하 이식 모델 간 FDG 친화력을 비교했다. 종양 성장 확인 및 포도당 수송체 1(GLUT1) 그리고 헥소키나아제 2(HK2)와 FDG 섭취 간 상관관계를 현미경적 관찰과 면역염색 활용하여 조사했다.

FDG-PET 결과가 있는 30례의 PDX의 RNA 시퀀싱 데이터를 이용하여 최대 표준섭취계수(SUVmax)와 연관된 유전자 지표를 식별했다. 5가지 유전자 지표(*PLS1*, *PYY*, *HBQ1*, *SLC6A5*, *NAT16*)를 이용하여 높은 FDG 섭취를 보이는 위암을 예측하는 모델(PETscore)를 구축했고, 환자에서 RNA-seq 과 qRT-PCR 기법을 통해 평가했다. 더욱이, 암유전체지도(TCGA) 및 아시아 암 연구 그룹(ACRG) 위암 공공데이터에서 모델의 특성을 조사했다.

결과: PET 촬영 프로토콜 150 μCi 의 용량을 주입하고, 1시간 뒤 촬영하는 것으로 결정했다. 동일 PDX 조직을 이용한 정위이식 및 피하 이식 마우스 모델 간 비교에서 정위이식 모델이 FDG섭취가 높았고, 종양 성장이 느렸다. 종양 세포 내 GLUT1과 HK2 발현의 H-score는

SUVmax와 상관관계를 보였다.

환자에서 PETscore는 실제 SUVmax값과 비교하여 유의한 예측 값을 제공했다. TCGA 및 ACRG 데이터를 이용한 조사에서 PETscore가 해당과정, 현미부수체 불안정성(MSI) 상태, 그리고 상피간엽이행(EMT) 관련 예후에 연관성을 보였다.

결론: 전임상적 위암 PDX 기반 [^{18}F]FDG-PET 프로토콜은 종양 특이적 FDG 섭취를 나타내고, 당대사 단백질과 상관관계를 보인다. PDX 이식 마우스모델은 위암에서 PET 활성 평가에 유용할 수 있다. FDG 섭취 예측 모델(PETscore)은 다양한 대사 프로파일 기반 위암의 분자적 특징을 제안한다. 더욱이, PETscore는 FDG 섭취를 예측하여 병기 및 관찰을 위한 개인맞춤 FDG-PET을 제안할 수 있을 것이다.

핵심어: 위암, 양전자 방출 단층 촬영, 환자유래이종이식, 유전자 지표, 표준섭취계수, 해당과정, 현미부수체 불안정성, 상피간엽이행

학번: 2017-34897